Net exchange parameterization of thermal infrared radiative transfer in Venus' atmosphere

V. Eymet,[1] R. Fournier,[1] J.-L. Dufresne,[2] S. Lebonnois,[2] F. Hourdin,[2] and M. A. Bullock[3]

Received 7 October 2008; revised 16 July 2009; accepted 4 August 2009; published 7 November 2009.

[1] Thermal radiation within Venus atmosphere is analyzed in close details. Prominent features are identified, which are then used to design a parameterization (a highly simplified and yet accurate enough model) to be used in General Circulation Models. The analysis is based on a net exchange formulation, using a set of gaseous and cloud optical data chosen among available referenced data. The accuracy of the proposed parameterization methodology is controlled against Monte Carlo simulations, assuming that the optical data are exact. Then, the accuracy level corresponding to our present optical data choice is discussed by comparison with available observations, concentrating on the most unknown aspects of Venus thermal radiation, namely the deep atmosphere opacity and the cloud composition and structure.

Citation: Eymet, V., R. Fournier, J.-L. Dufresne, S. Lebonnois, F. Hourdin, and M. A. Bullock (2009), Net exchange parameterization of thermal infrared radiative transfer in Venus' atmosphere, *J. Geophys. Res.*, *114*, E11008, doi:10.1029/2008JE003276.

1. Introduction

[2] In the past decades, General circulation models (GCMs) have become central tools for the study of the Earth climate and operational weather forecast. Because those numerical tools are mainly based on physics laws, they can be in principle adapted quite easily to various planetary atmospheres, by changing in particular fundamental parameters such as the planetary radius, the gas heat capacity, etc. Some specific processes must also be included depending on the planet such as the presence of ocean and of vegetation on Earth, the CO_2 condensation on Mars, or the presence of photochemical haze surrounding the atmosphere on Titan [*Hourdin et al.*, 1995; *Forget et al.*, 1999; *Richardson et al.*, 2007]. However, a major step in this process is generally the development of a radiative transfer code. Because of the complexity of radiative transfer computation, and because heating rates must be computed typically a few times per hour for simulations covering decades or centuries, at each mesh of a grid of typically a few tens of thousands of points, such codes (named radiative transfer parameterizations) must be based on highly simplified algorithms that are generally specific to the particular atmosphere.

[3] From this point of view, the case of Venus is quite challenging. With its deep atmosphere of CO_2 (92 bars at the surface), its huge greenhouse effect (735 K at surface), its H_2SO_4 clouds which in some spectral regions behave as pure scatterers, allowing to "see" through the clouds in some near infrared windows [*Allen and Crawford*, 1984; *Bézard et al.*, 1990], and because part of the spectral properties are not measured or constrained in the conditions encountered there, Venus is even a problem for making reference computations with line-by-line codes.

[4] A full description of the energy balance of the atmosphere of Venus can be found in the work of *Titov et al.* [2007]. A large fraction of the solar flux is reflected by the clouds, allowing the absorption by the atmosphere of only approximately 160 W m^{-2} on average. Only 10% of the incident solar flux reaches the surface. Because of the thickness of the atmosphere in most of the infrared, most of the outgoing thermal radiation comes from the cloud top. Below clouds, the deeper atmosphere can only radiate to space in the near-infrared windows. The huge infrared opacity in that region induces a strong greenhouse effect that can explain the extremely hot surface temperature. In this region, energy is radiatively transported through short-range radiative exchanges. Convection, essentially located in the lower and middle clouds (from roughly 47–50 km to around 55 km altitude), has been identified thanks to the stability profiles measured by Pioneer Venus and Venera entry probes [*Schubert*, 1983]. This convection certainly plays a role in transporting energy from the base of the clouds (heated from below by the deep atmosphere) to the upper clouds, where infrared radiation is able to reach space. This one-dimensional description of the energy balance is a global average view, and its latitudinal variations is related to the dynamical structure of the atmosphere, the description of which is the main goal of a General Circulation Model.

[5] In order to perform reference infrared computations and to develop a fast algorithm suitable for a GCM, we make use of the Net Exchange Rate (NER) formalism based on ideas originally proposed by *Green* [1967] and already used to derive a radiation code for the LMD Martian GCM [*Dufresne et al.*, 2005], or to analyze the radiative exchanges on Earth [*Eymet et al.*, 2004]. In the NER

[1]Laboratoire Plasma et Conversion de l'Energie, CNRS-UPS, Toulouse, France.
[2]Laboratoire de Météorologie Dynamique-IPSL, CNRS-UPMC, Paris, France.
[3]Department of Space Studies, Southwest Research Institute, Boulder, Colorado, USA.

0148-0227/09/2008JE003276

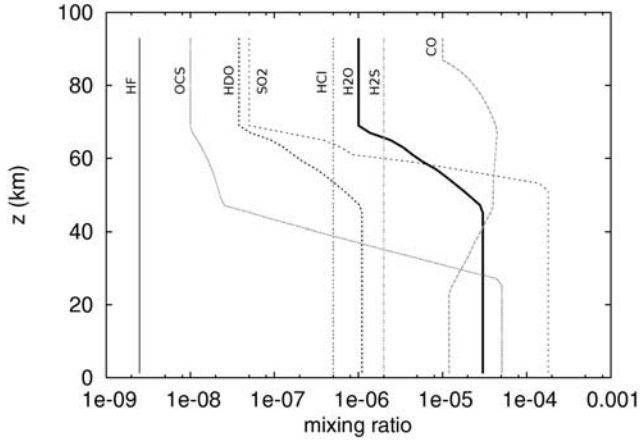

Figure 1. Mixing ratio of gaseous active species, as function of altitude (km).

approach, rather than computing the radiative budget as the divergence of the radiative flux, this budget is computed from the radiative net exchanges between all the possible pairs of elements *A* and *B*, defined as the difference of the energy emitted by *A* and absorbed by *B* and that emitted by *B* and absorbed by *A*. Using the plane parallel approximation, net radiative exchanges to be considered are those between two atmospheric layers, between a surface and an atmospheric layer (space being considered as a particular "surface" at 0 K) or between the two surfaces (ground and space). This formalism insures some important properties such as the reciprocity principle and the energy conservation whatever the retained numerical assumptions [*Dufresne et al.*, 2005]. Thus drastically different levels of approximation can be applied to various terms of the computation, without violating those fundamental physical principles.

[6] Within the GCM, the radiative transfer is divided in solar radiative forcing, and thermal radiation energy redistribution (and cooling to space). This paper describes exclusively how we use the NER formalism to compute thermal radiation, and how this computation is parameterized for use within the GCM. This is only a first step, since we need also to compute the solar radiative forcing with consistent input parameters (essentially the cloud structure and optical properties) to get a fully consistent radiative scheme in the GCM. However, for the moment, the solar forcing in the GCM is taken from computations by *Crisp* [1986], or by *Moroz et al.* [1985] and *Tomasko et al.* [1980]. The development of a parameterization of solar forcing is a work in progress, and will be published in a future paper.

[7] In section 2, a set of referenced optical data is chosen and briefly described for all components of Venus atmosphere, and these optical data are used to perform reference net exchange simulations. The corresponding net exchange matrices are then physically interpreted, in order to highlight the features that will serve as start basis for the parameterization design. This parameterization is described and validated in section 3. In the validation process, accuracy is checked against reference Monte Carlo simulations assuming that all optical data are exact. This means that, at this stage, the parameterization methodology (the retained physical pictures, the formulation choices) is validated. In particular, we can confidently extrapolate that no further technical developments will be required if we want to include more accurate optical data that may arise from a better knowledge of the spectral characteristics and composition of the atmosphere of Venus. However, we need to discuss the level of confidence associated to our present optical data against available observations in order to allow an immediate use of the proposed parameterization in Venus GCMs [*Lebonnois et al.*, 2005, 2006]. This discussion is the object of section 4, in which a particular attention is devoted to the collision induced continuum model and the composition and vertical structure of the cloud.

2. Reference Net Exchange Simulations

2.1. Gas Spectroscopic Data

[8] The temperature at ground level on Venus is 735 ± 3 K for a ground pressure of 92 ± 2 bar. The lower atmosphere is composed mainly of CO_2 (96.5%) and N_2 (3.5%) that are well mixed over the whole atmosphere. In addition, Venus' atmosphere includes several chemically active species: H_2O, CO, OCS, SO_2, HCl and HF. Figure 1 displays the concentrations used in our simulations. These concentrations were used by *Bullock and Grinspoon* [2001] to compute the k coefficients used in our study. Though these values are close to published composition data [*von Zahn and Moroz*, 1985; *Taylor et al.*, 1997; *de Bergh et al.*, 2006; *Bézard and de Bergh*, 2007], an update of these profiles with a new computation of k coefficients is needed to improve this part of our computation. In particular, more recent observations are becoming available from the Venus Express mission, both in the mesosphere [*Belyaev et al.*, 2008; *Fedorova et al.*, 2008] and in the deep atmosphere [*Marcq et al.*, 2008], which should help define future reference profiles.

[9] In the infrared domain, gaseous absorption is mainly due to rotation-vibration absorption lines of CO_2, H_2O, SO_2, CO, OCS, HDO, H_2S, HCl and HF. Because of the large pressure variations with altitude, line widths are strongly dependent on altitude: from very narrow isolated lines at the top of the atmosphere, to extremely wide lines with strong line overlap in the deep atmosphere (see Figure 2). At each altitude and for the considered spectral interval, the average value $\bar{k}_a$ of the absorption coefficient and the overlap parameter Φ are also shown in Figure 3. The overlap parameter Φ is defined as $\Phi = \frac{\bar{k}_a^{\,2}}{\bar{k}_a^2 - \bar{k}_a^{\,2}}$ where $\bar{k}_a^2 - \bar{k}_a^{\,2}$ is the variance of the absorption coefficient within the spectral interval. The variation of Φ with altitude is shown, for instance, in the [4700–4900] cm^{-1} spectral interval (values of Φ may be different in a different spectral interval). Spectral lines are well separated at high altitude and the overlap parameter Φ is small compared to unity (Figures 2a and 2b). Pressure broadening increases lines overlap at middle altitudes (Figure 2c) and, at the bottom of the atmosphere, lines can no longer be identified.

[10] In the following simulations and quantitative analysis, gas absorption opacities are those of *Bullock and Grinspoon* [2001]. These opacities were generated from high-resolution spectral data for the nine main molecular species corresponding to a combination of the HITRAN1996 and HITEMP line-by-line databases [*Rothman et al.*, 2000, 2003]. Continuous absorption line spectra at each of 81 altitudes are reduced to discrete *k* distribution data sets

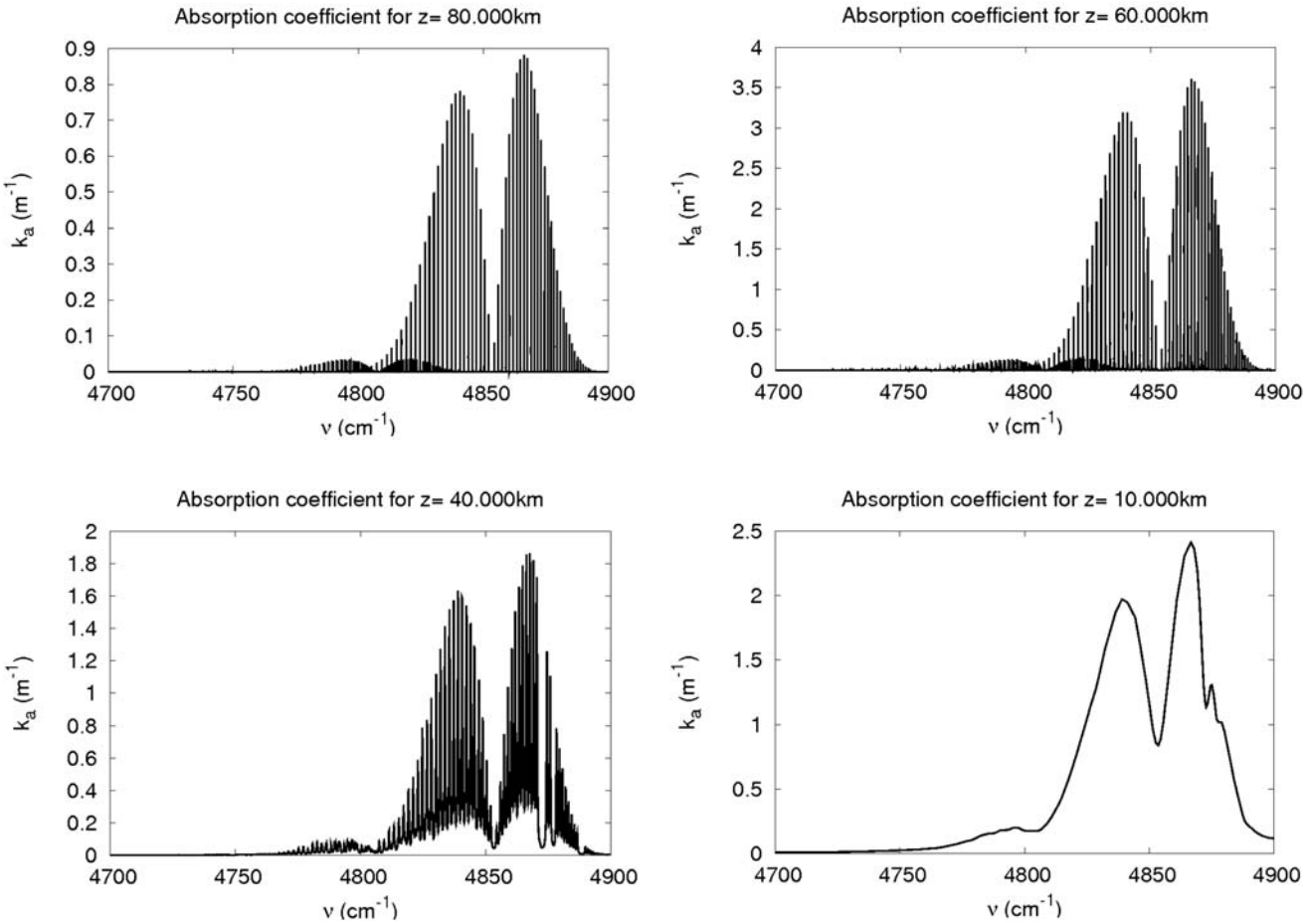

Figure 2. Absorption coefficient k_a (m^{-1}) as a function of wave number (cm^{-1}) in the [4700–4900] cm^{-1} (2.04–2.13 μm) spectral interval: at an altitude of (a) 80 km, (b) 60 km, (c) 40 km, and (d) 10 km. The overlap parameter Φ and the average value $\bar{k_a}$ of the absorption coefficient for this spectral interval are given underneath each figure.

[*Goody et al.*, 1989; *Lacis and Oinas*, 1991] on the basis of a narrow band spectral discretization and a 8 points Gaussian quadrature. The infrared spectrum from 1.71 to 250 μm (40 to 5700 cm^{-1}) is covered with 68 narrow bands. A description of the corresponding spectral mesh can be found in Table A1 (Appendix A). The vertical grid is regular: each atmospheric layer is 1 km thick from the ground up to an altitude of 61 km, and layers above this altitude are 2 km thick. In order to account for the variation with temperature of line intensities and line profiles, three distinct k distribution data sets have been computed: a primary set corresponding to the VIRA temperature profile (refereed to as T^{VIRA}) and two sets corresponding to a uniform 10 K increase and decrease (T^{VIRA} + 10 K and T^{VIRA} − 10 K respectively).

[11] Because of the high pressure and temperature levels encountered in Venus atmosphere, collisions between gas molecules induce significant additional opacities. Compared with standard absorption line spectra, these opacities evolve slowly with frequency and they are commonly referred to as "collision-induced continuum." This phenomenon is accurately quantified for Earth atmosphere, but remains widely unknown as far as Venus atmosphere is concerned. Hereafter, we only consider CO_2-CO_2 collisions and we make use of modeling results from A. Borysow (http://www.astro.ku.dk/~aborysow) for the [10, 250] cm^{-1} spectral range [*Gruszka and Borysow*, 1997] together with available empirical data for the [250, 4740] cm^{-1} spectral range [*Moskalenko et al.*, 1979] (continuum is set to zero between 4740 and 5825 cm^{-1}). Another effect of high pressures is to be found in the sub-Lorentzian nature of CO_2 absorption lines: absorption in far wings is less than predicted by standard Lorentz pressure-broadened lines [*Burch et al.*, 1969]. Correction factors are commonly used to account for this phenomenon [*Bézard et al.*, 1990; *Perrin and Hartmann*, 1989], in particular in the so-called "spectral windows" (mainly at 1.73 and 2.30 μm), but not enough experimental data are available to allow quantitative evaluations throughout the all infrared spectrum, as required for the present study. We therefore introduce no specific modification of the k distribution data set from the work of *Bullock and Grinspoon* [2001], keeping in mind that line profiles were truncated at 25 cm^{-1} from line center during its production.

[12] Note that H_2O collision-induced continuum (*Roberts et al.* [1976], as presented in *Bullock* [1997]), and Rayleigh scattering by CO_2 and N_2 with temperature and pressure dependence of the real refraction index from the International Critical Tables [*Washburn et al.*, 1930] have also been

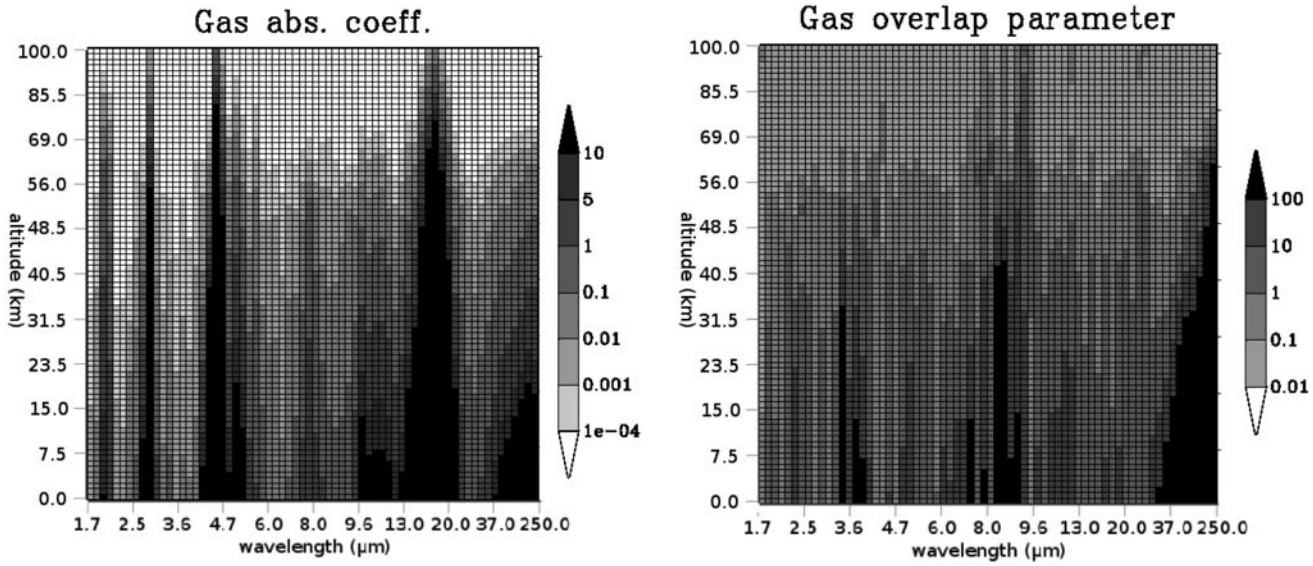

Figure 3. (a) T^{VIRA} average gaseous absorption coefficient $\bar{k}_a$ (m^{-1}), as a function of wavelength and altitude. Including CO_2 collision-induced absorption. The spectral interval ranges from 1.71 to 250 μm (40–5700 cm^{-1}) with a nonconstant bandwidth (Table A1). (b) Gaz overlap parameter Φ.

included. Both phenomena have been shown to be negligible for the purposes of the present study.

2.2. Clouds and Hazes Opacities

[13] Venus is completely shrouded by clouds in the 47 to 70 km altitude region. Middle latitude clouds vertical structure and composition is known since measurements by Venera 9 and 10 landers, and the four entry probes from Pioneer Venus [*Esposito et al.*, 1983].

[14] Cloud droplets are constituted by H_2SO_4/H_2O aerosols [*Pollack et al.*, 1978]. Four different particle modes have been identified and their size distributions can be modeled with truncated lognormal distributions [*Zasova et al.*, 2007; *Esposito et al.*, 1983; *Knollenberg and Hunten*, 1980]. We retain here the modal properties and the nominal number densities of *Zasova et al.* [2007] (see Tables 1 and 2) that are given in the 48 to 84 km altitude region. These cloud microphysical data and the complex refractive index of H_2SO_4 solutions [*Palmer and Williams*, 1975] are used together with the Mie theory in order to compute the optical data required for radiative transfer computations: total extinction optical depths, single-scattering albedo and phase functions. The detailed phase function is not directly used. Instead, the phase function asymmetry parameter is computed on the basis of the exact Mie phase function and radiative transfer simulations are performed using the Henyey-Greenstein phase function [*Goody and Yung*,

Table 1. Nominal Cloud Model Data, Originally Taken From *Zasova et al.* [2007][a]

	Mode 1	Mode 2	Mode 2′	Mode 3
$\bar{r}$ (μm)	0.15	1.05	1.40	3.85
$\sigma_{\log}$	1.91	1.21	1.23	1.30
H_2SO_4 mass %	84.5	84.5	84.5	84.5

[a]The size distribution of each particle mode is described by a lognormal distribution of modal radius $\bar{r}$, logarithmic width $\sigma_{\log}$ (see Appendix B) and a mass percentage of sulfuric acid.

Table 2. Nominal Particle Densities (cm^{-3}) Used in the Lognormal Size Distribution of Cloud Droplets[a]

$z_{\max}(i)$ (km)	$z_{\min}(i)$ (km)	$N_0(1)(i)$	$N_0(2)(i)$	$N_0(2')(i)$	$N_0(3)(i)$
84.000	83.000	1.8	0.	0.	0.
83.000	82.000	2.5	0.	0.	0.
82.000	81.000	4.	0.	0.	0.
81.000	80.000	6.	0.	0.	0.
80.000	79.000	10.	1.	0.	0.
79.000	78.000	15.	1.5	0.	0.
78.000	77.000	20.	2.	0.	0.
77.000	76.000	30.	3.	0.	0.
76.000	75.000	50.	5.	0.	0.
75.000	74.000	70.	7.	0.	0.
74.000	73.000	110.	11.	0.	0.
73.000	72.000	160.	16.	0.	0.
72.000	71.000	240.	24.	0.	0.
71.000	70.000	360.	36.	0.	0.
70.000	69.000	530.	53.	0.	0.
69.000	68.000	800.	80.	0.	0.
68.000	67.000	1200.	120.	0.	0.
67.000	66.000	1800.	180.	0.	0.
66.000	65.000	1500.	150.	0.	0.
65.000	64.000	200.	0.	20.	0.
64.000	63.000	750.	0.	75.	0.
63.000	62.000	750.	0.	75.	0.
62.000	61.000	750.	0.	75.	0.
61.000	60.000	750.	0.	75.	0.
60.000	59.000	500.	0.	30.	0.
59.000	58.000	500.	0.	50.	0.
58.000	57.000	500.	0.	50.	0.
57.000	56.000	300.	0.	50.	0.
56.000	55.000	500.	0.	50.	3.
55.000	54.000	500.	0.	50.	10.
54.000	53.000	500.	0.	50.	10.
53.000	52.000	500.	0.	50.	10.
52.000	51.000	500.	0.	50.	10.
51.000	50.000	500.	0.	50.	20.
50.000	49.000	500.	0.	50.	30.
49.000	48.000	500.	0.	50.	20.

[a]Nominal particle densities are defined for 36 layers. Layer i extends from $z_{\min}(i)$ to $z_{\max}(i)$ (for each particle mode). See Appendix B for a description of the lognormal distribution.

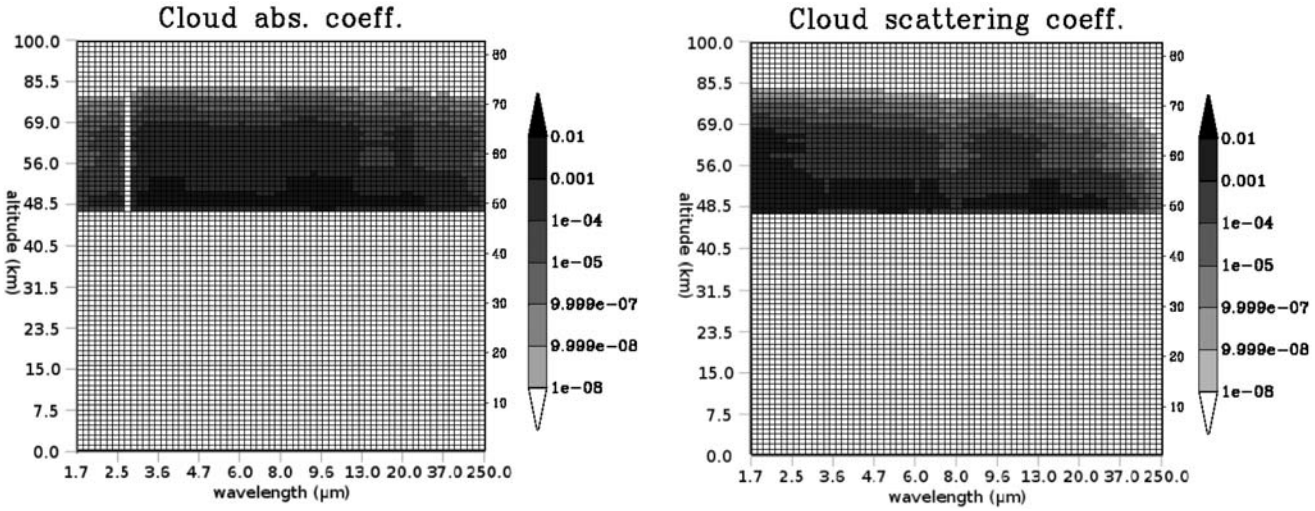

Figure 4. (a) Cloud absorption coefficient (in m^{-1}) and (b) cloud scattering coefficient (in m^{-1}), as function of wavelength and altitude.

1995]. Details of the clouds optical depths computation can be found in Appendix B. Figure 4 displays absorption and scattering coefficients while Figure 5 shows single-scattering albedo and asymmetry parameter as function of narrow band interval and atmospheric layer index. Note in particular that the single-scattering albedo takes values very close to unity in the near-infrared ($\lambda < 2.5$ μm), making the clouds translucent and allowing thermal radiation from below to escape in the CO_2 spectral windows.

2.3. Monte Carlo Simulations and Net Exchange Rate Analysis

[15] The code KARINE (http://web.lmd.jussieu.fr/~eymet/karine.html) is used together with the above presented gas and cloud spectral databases to produce reference radiative transfer simulation results. This code is based on a Net Exchange Monte Carlo algorithm. We will not describe here the details of such algorithms, that were first introduced in the work of *Cherkaoui et al.* [1996] and were gradually refined in the last decade, in particular as far as atmospheric applications are concerned. In the present context, it is particularly meaningful to point out the specific convergence difficulties associated with extremely high optical thicknesses, for which practical solutions were proposed recently, first for purely absorbing media [*De Lataillade et al.*, 2002] and then for simultaneous high absorption and high scattering conditions [*Eymet et al.*, 2005]. KARINE implements all such methodological developments and was submitted to a systematic validation procedure against the corresponding benchmark solutions. Multiple scattering accurate representation was controlled with a specific attention using the invariance properties of *Blanco and Fournier* [2003] and *Roger et al.* [2005].

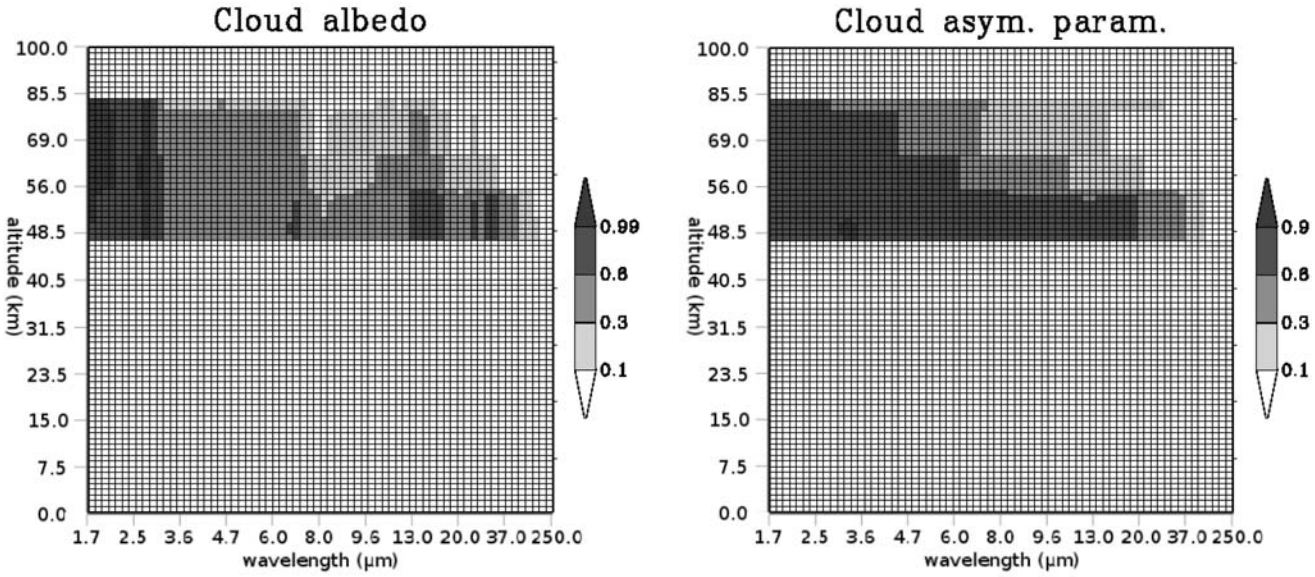

Figure 5. (a) Cloud single-scattering albedo and (b) cloud asymmetry parameter, as function of wavelength and altitude.

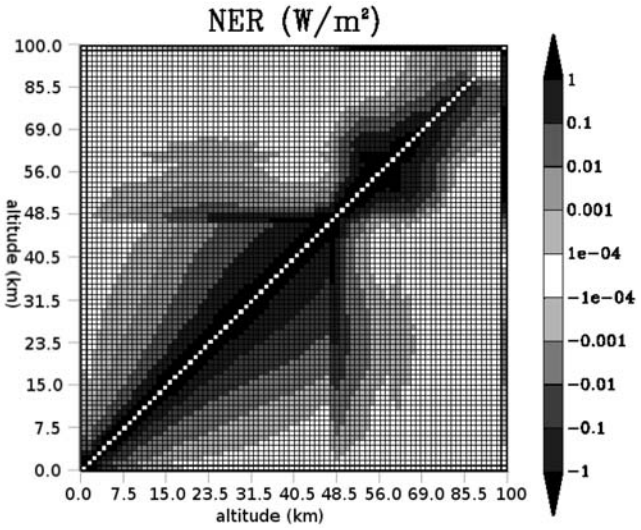

Figure 6. Spectrally integrated Net Exchange Rate matrix. The NER between atmospheric layers i and j is located at the intersection between row index i and column index j. The first row represents NERs between the ground and every atmospheric layer (ground heating). These NERs have a negative sign because the ground is cooled by radiative exchanges with the atmosphere. The last row represents NERs between all atmospheric layers and space (cooling to space). These NERs are positive because space is heated by radiative exchanges with the atmosphere.

[16] Each radiative transfer simulation (and later, each parameterization call) produces a Net Exchange Rate (NER) matrix associated with the atmospheric vertical discretization plus ground and space. The NER $\Psi(i, j)$ between two elements i and j of the atmosphere (an element can be an atmospheric layer, ground or space) is defined as $E(j \rightarrow i)$, the radiative power emitted by element j and absorbed by element i, minus $E(i \rightarrow j)$, the radiative power emitted by element i and absorbed by element j [*Dufresne et al.*, 2005; *Green*, 1967; *Joseph and Bursztyn*, 1976]. In the plane parallel approximation, each NER between two atmospheric layers (or a layer and surface) has the dimension of a power per surface unity (W/m^2). The radiative budget $\zeta(i)$ of element i is then the sum of NERs between i and every other element j:

$$\Psi(i,j) = E(j \rightarrow i) - E(i \rightarrow j) \tag{1}$$

$$\zeta(i) = \sum_{j=0}^{m+1} \Psi(i,j) \tag{2}$$

[17] The purpose of the present section is to physically analyze these NER matrices. To avoid meaningless noisy structures, the NER analysis are performed on the basis of a smoothed T^{VIRA} profile. As the lower atmosphere is highly absorbing, IR radiative transfer has Rosseland-like diffusive features and fluctuations on a discretized temperature profile induce apparent second order spatial derivatives that translate into strong net exchanges between adjacent layers: a third order polynomial adjustment is made between the surface and altitude $z = 43$ km on the basis of the original VIRA temperature profile (the maximum temperature difference between T^{VIRA} and the adjusted profile is $\Delta T_{\max} = 2.5$ K). Figure 6 displays the matrix of spectrally integrated NERs for this smoothed temperature profile. NERs between a given atmospheric layer i and all other layers j can be found on line index i. The line index 0 corresponds to ground, and line $m + 1 = 82$ to space. Let us take the example of layer number 30: elements of line number 30 show first the NER between layer 30 and ground, then NERs between layer 30 and the 29 first atmospheric layers. These NER are positive: layer number 30 is heated by these 29 first layers because layer 30 is colder than layers below it. By definition, NER between layer 30 and itself is null. Subsequent elements correspond to NERs between layer 30 and atmospheric layers located above it, and the NER between layer 30 and space. These latter NERs are negative because layer 30 is warmer than all above layers. The NER matrix is antisymmetric because by definition $\Psi(j, i) = -\Psi(i, j)$, and all diagonal elements are null: $\Psi(i, i) = 0$.

[18] The amplitude of a given NER between two elements i and j is the result of the following combined effects [*Eymet et al.*, 2004; *Dufresne et al.*, 2005]:

[19] 1. Temperature difference between i and j: the greater the temperature difference, the greater the absolute value of the NER $\Psi(i, j)$;

[20] 2. Local emission/absorption properties of i and j: maximum emission/absorption is reached when i or j behave like a blackbody, which is the case when i or j is either the ground surface, space or an optically thick atmospheric layer (especially if the layer is cloudy);

[21] 3. Attenuation of radiation along the optical paths between i and j: it depends on absorption properties of the intermediate atmosphere, distance between i and j, complexity of the optical path domain in particular as far as multiple scattering is concerned.

[22] In the case of Venus atmosphere, the temperature difference is quite easy to picture: roughly speaking the greater the distance between i and j, the greater the temperature difference. The two other points are more subtle because their influences are opposite as function of absorption properties when i and/or j are gas layers: at frequencies where the atmospheric gas is a strong absorber, the emission is strong, which increases the NERs involving gas layers, but attenuation is also strong which decreases all types of distant NERs. The strong spectral dependence of gaseous absorption (within or outside absorption bands, at the center or at the wings of absorption lines) is therefore essential when physically analyzing the structure of the NER matrix of Figure 6. Let us for instance consider the NERs between gas layers in the deep atmosphere. Each gas layer can only exchange radiation with its close neighbors. For further layers, although the temperature difference is greater, attenuation is too strong for significant net exchanges to occur. Above 10 km (layer index 12), although attenuation seems very strong from this point of view, net exchanges are observed with the bottom of the cloud (layers 49–50). This requires that these two types of net exchanges (with close neighbors and with cloud bottom) occur at different frequencies within a given spectral band. The fact that NERs with the cloud are observed is due to absorption by cloud

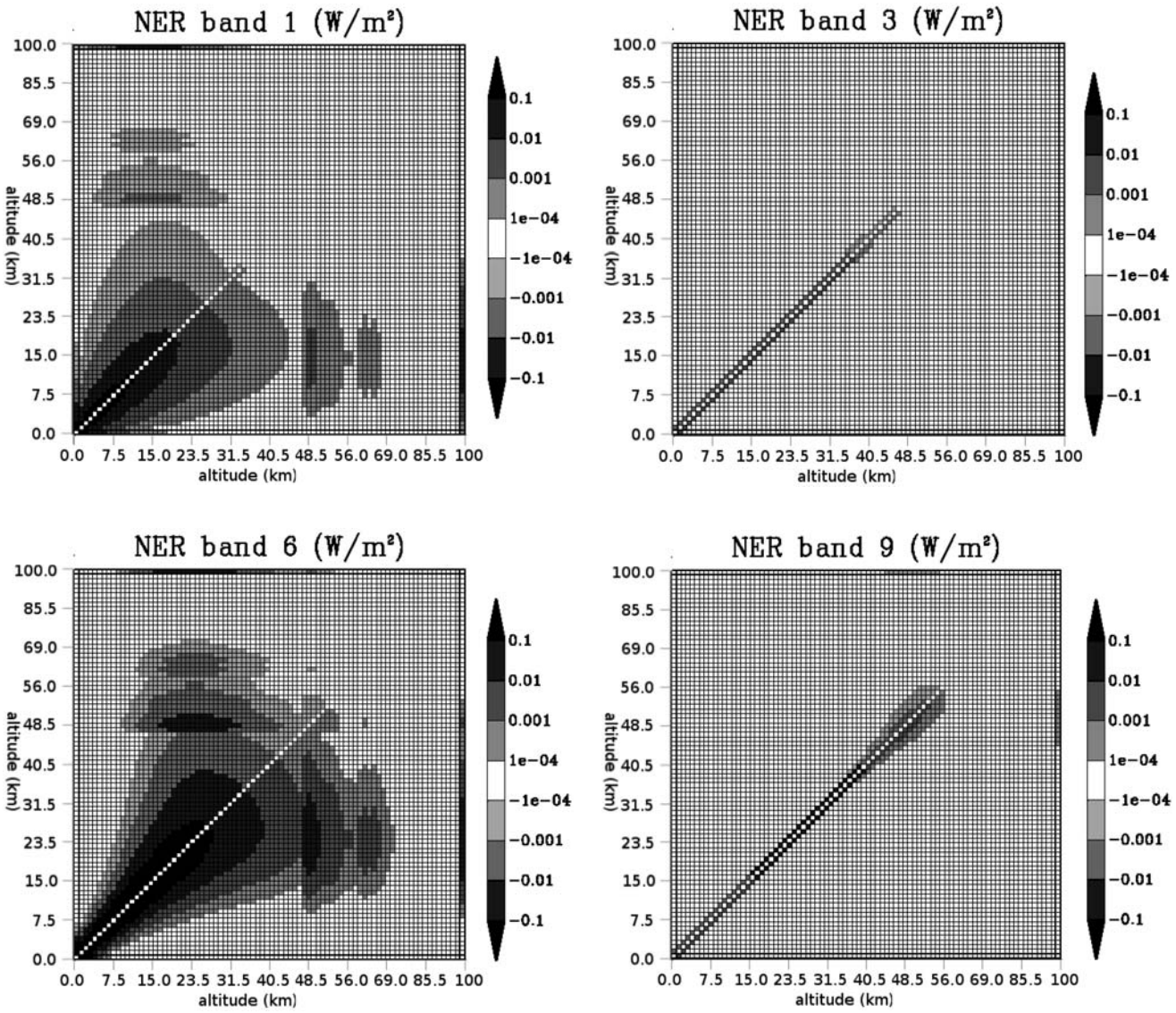

Figure 7. NER matrixes in selected narrow bands: (a) narrow band number 1, extending from 5700 to 5825 cm^{-1} (1.71–1.75 μm); (b) narrow band number 3, 4950–5200 cm^{-1} (1.92–2.02 μm); (c) narrow band number 6, 4134–4350 cm^{-1} (2.30–2.42 μm); (d) narrow band number 9, 3760–3875 cm^{-1} (2.58–2.66 μm).

droplets at frequencies where the atmospheric gas alone would be quite transparent. The interpretation of the structure of the NER matrix requires therefore to keep in mind the band structure of gaseous absorption (see Figure 3), the separated line structure within each band when pressure broadening is not too strong (see Figure 2) and the regularity of cloud absorption spectra (see Figure 4). The main features of Figure 6 are the following:

[23] 1. Net exchanges between the ground (layer 0) and atmospheric layers is only significant for the first layers. This is due to the extremely large opacities corresponding to 92 bars of CO_2 at 700 K. Pressure broadening is such that gaseous absorption lines are strongly overlapped (see Figure 2d), and no transmission at frequencies between lines centers is possible: the gas behaves like an optically thick gray medium in each narrow band, as indicated by the large values of the overlap parameter in Figure 3b.

[24] 2. Strong NERs are observed between neighboring layers up to 65 km. These intense NERs, despite of small temperature differences (short distance NERs), indicate that even at moderate pressures where the density of gaseous absorbers decreases, emission and absorption are still very strong at the center of the most intense absorption lines.

[25] 3. Long distance NERs between atmospheric layers are weak (the NER matrix is very much empty), except as far as cloud layers are concerned (because of the continuous absorption by cloud droplets).

[26] 4. NERs with space are significant within and above the cloud region. This can be analyzed similarly as the effect of cloud bottom for the deep atmosphere: space is a ''continuous absorber'' that allows long distance net exchanges in all spectral windows of moderate gaseous absorption. This effect is particularly strong because space is at 3 K and therefore temperature difference is large.

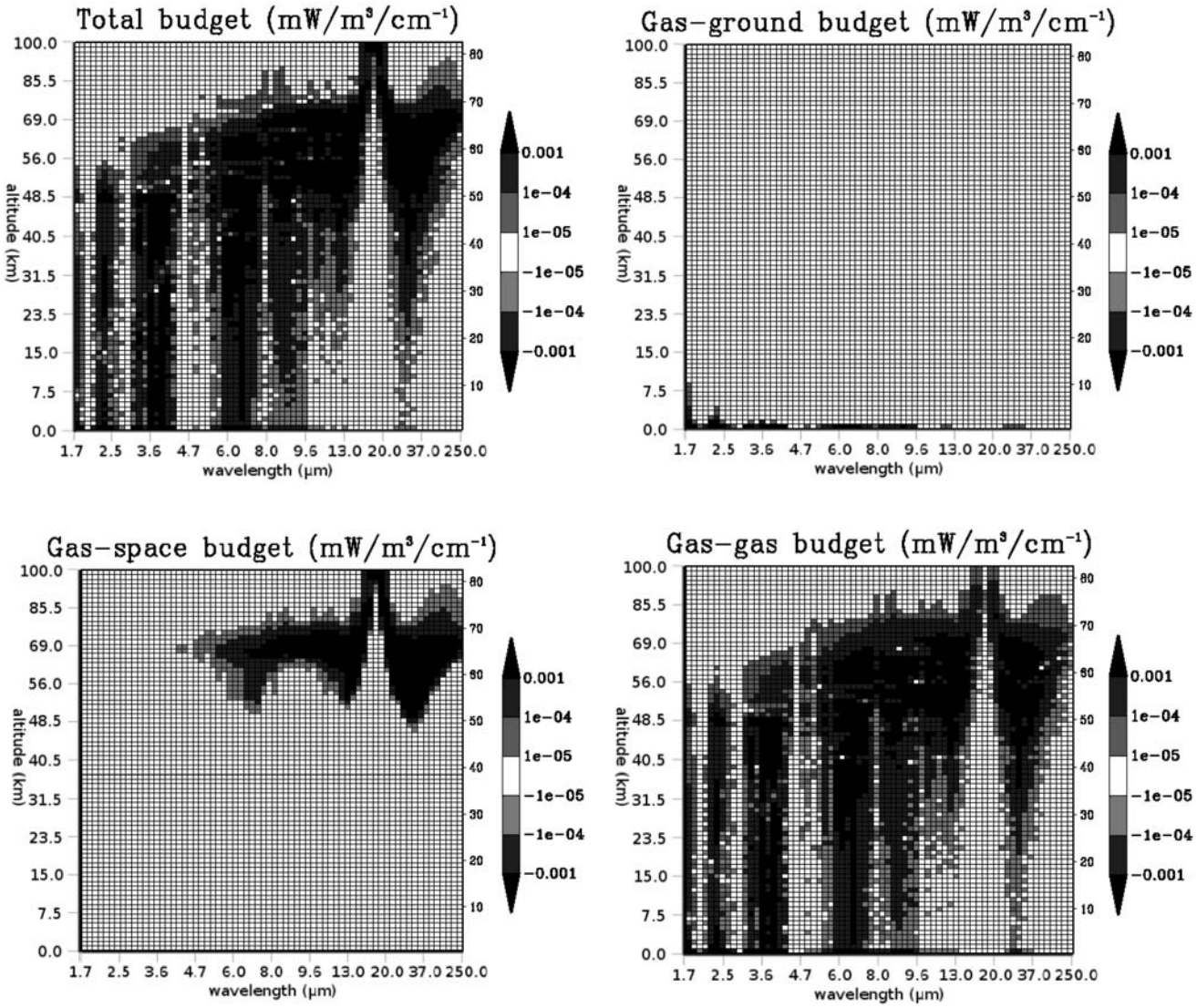

Figure 8. (a) Total radiative budget per cubic meter ($\zeta_{nb}(i)/\Delta z_i$, where Δz_i is the thickness of layer i), as a function of wavelength and altitude. This total radiative budget is then decomposed in (b) net exchanges with the ground, (c) net exchanges with space, and (d) net exchanges between atmospheric layers.

[27] Further illustration of these mechanisms can be performed on the basis of partial NER matrices corresponding to selected narrow bands. Figures 7a and 7c display the NER matrices corresponding to narrow bands indices 1 and 6, that respectively cover the 1.73 μm and 2.30 μm spectral windows. Net exchanges between space and deep atmospheric layers (and even the ground) are clearly visible, as well as net exchanges between distant atmospheric layers within the deep atmosphere. Almost all NERs between space and the deep atmosphere occur in these two bands, which is the reason of their very specific role in terms of observations. Bands indices 3 and 9 (Figures 7b and 7d) are very different: optical thicknesses are high, and net exchanges are strictly restricted to immediately adjacent gas layers.

[28] For each narrow band, the total radiative budget of layer i in narrow band index nb

$$\zeta_{nb}(i) = \sum_{j=0}^{m+1} \Psi_{nb}(i,j) \tag{3}$$

can be decomposed also as

$$\zeta_{nb}(i) = \zeta_{nb}(i)^{atm-ground} + \zeta_{nb}(i)^{atm-space} + \zeta_{nb}(i)^{atm-atm} \tag{4}$$

where $\zeta_{nb}(i)^{atm\text{-}ground} = \Psi_{nb}(i, 0)$ is the net heating of layer i by the ground, $\zeta_{nb}(i)^{atm\text{-}space} = \Psi_{nb}(i, m + 1)$ is the opposite of the cooling to space of layer i and $\zeta_{nb}(i)^{atm\text{-}atm} = \sum_{j=1}^{m} \Psi_{nb}(i, j)$ is the portion of the radiative budget that is due to net exchanges between atmospheric layer i and the rest of the atmosphere. Figure 8 displays these three contributions and the total radiative budget as function of wavelength and layer index i. In all figures displaying radiative budgets of atmospheric layers, results are presented in W/m^3, corresponding to $\zeta_{nb}(i)/\Delta z_i$, where Δz_i is the thickness of layer i. This allows quantitative comparisons independently of the vertical discretization. This transformation cannot be used when analyzing Net exchange matrices (see Figures 6 and 7 where results are presented in W/m^2), because each net exchange involves two atmospheric layers. It appears that:

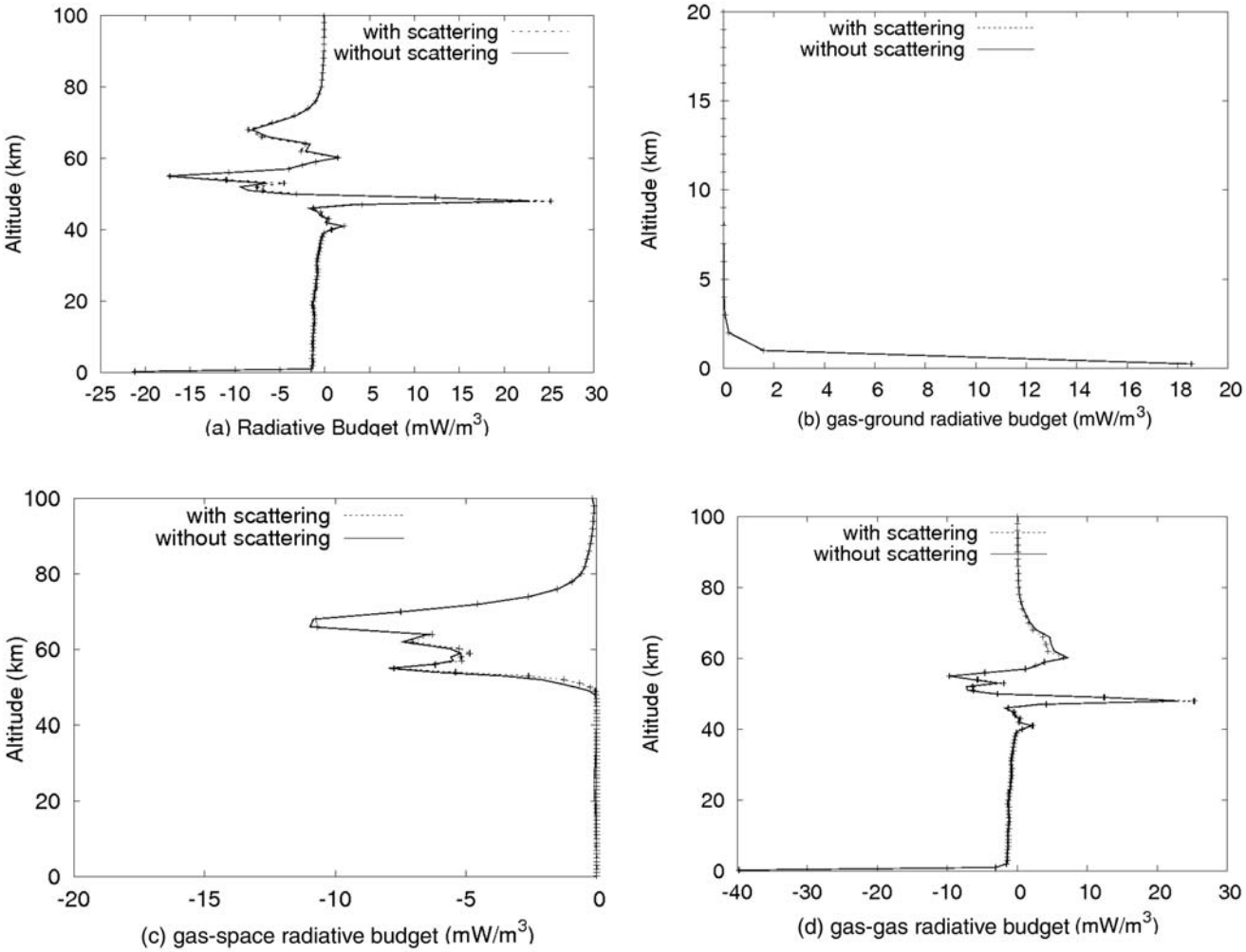

Figure 9. Spectrally integrated radiative budget in mW/m^3 ($\zeta_{nb}(i)/\Delta z_i$, where Δz_i is the thickness of layer i) computed with and without scattering. The total radiative budget (a) is decomposed in (b) portion of the budget due to exchanges with the ground, (c) portion of the budget due to exchanges with space, and (d) portion of the budget due to exchanges between atmospheric layers.

[29] 1. $\zeta_{nb}(i)^{atm\text{-}ground}$ (Figure 8b) is null, except at the very bottom of the atmosphere.

[30] 2. $\zeta_{nb}(i)^{atm\text{-}space}$ (Figure 8c) is null for the whole deep atmosphere (except in the near-infrared windows where cooling to space occurs but is small compared with atm-atm exchanges) but the whole atmosphere above the clouds is significantly cooled by radiative exchanges with space. Cooling to space also occurs within the upper cloud and partially at the lower cloud levels through the rest of the cloud in some far-infrared spectral bands.

[31] 3. $\zeta_{nb}(i)^{atm\text{-}atm}$ (Figure 8d) is the dominant part of the radiative budget, except near the surface and far above clouds. Generally speaking, the upper atmosphere is heated by the deep atmosphere (which is reciprocally cooled by the same mechanism). atm-atm net exchanges remain dominant above the clouds, in a region where the atmosphere is optically thin enough for $\zeta_{nb}(i)^{atm\text{-}space}$ to be very significant in this very same region. However again, this is due to the line structure of gaseous absorption: short distance atm-atm net exchanges occur at frequencies close to line centers, while long distance atm-space net exchanges are associated with line wing frequencies. Similar reasons lead to a atm-atm net radiative cooling of most of the cloud (net exchange with the upper part of the cloud and the top atmosphere) that is comparable in magnitude with cooling to space. Also, very remarkable is the strong heating of the bottom of the cloudy region (layers 48–49) due to net exchanges with the atmosphere below. Atm-atm net exchanges are also significant in the deep atmosphere.

[32] The resulting vertical structure of the total radiative budget integrated over the whole spectrum is displayed in Figure 9. Cooling to space dominates in the upper atmosphere (above 70 km), as well as in the upper cloud region (57 to 70 km), with a marked maximum at 57 km (corresponding to the upper limit of the dense cloud region). Within the dense cloud region (from 49 to 57 km) the net effect of atm-space and atm-atm net exchanges is an overall net cooling of the upper part, and a heating of the lower part (with a comparable magnitude). In the center part of the dense cloud region, the structure of the radiative budget

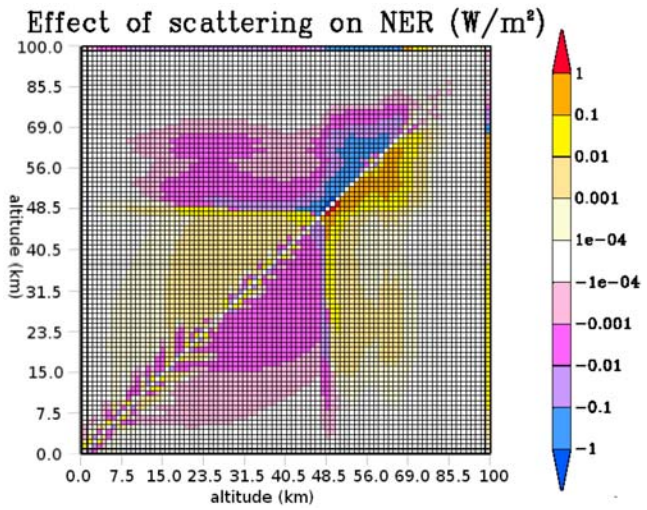

Figure 10. Spectrally integrated matrix of the effect of scattering on net exchange rates. This figure represents $d\Psi(i, j) = \Psi(i, j) - \Psi^{aa}(i, j)$, with $\Psi(i, j)$, the reference spectrally integrated NER between layers i and j, and $\Psi^{aa}(i, j)$, the spectrally integrated NER between layers i and j, computed within the absorption approximation (analytical result in a scattering-free atmosphere).

vertical profile is quite complex, and is very sensitive to the temperature profile, which itself controls the balance between solar heating, thermal exchanges and convection. The same observation could be made in the deep atmosphere. In both cases, short distance atm-atm exchanges are dominant, which means that the energy redistribution process associated with radiation is close to a diffusion process: the medium is optically thick in terms of absorption and a diffusive model such as Rosseland model is well adapted to the representation of the combined effects of emission, absorption and scattering. In such a model, the total radiative budget is proportional to the second derivative of the temperature profile with altitude, and the present discretization in $m = 81$ layers, associated with the uncertainties of the T^{VIRA} temperature profile, leads to strong fluctuations of this second order derivative. These fluctuations are clearly visible in the middle of the cloud layer. Note that when vertical energy exchanges are dominated by those local radiative exchanges, the temperature adjusts so that the fluctuations disappear; but in the present uncoupled study, the exchanges would have been dominated by those fluctuations if T^{VIRA} had not been smoothed below 43 km.

[33] Finally, we show in Figure 10 displays the differences between each reference NER (Figure 6), and NERs computed using the absorption approximation: absorption optical thicknesses are unchanged, while both particulate scattering optical thicknesses and Rayleigh scattering optical thicknesses are set to zero. Scattering affects net exchanges between the base of the clouds and the atmosphere underneath: radiation emitted in the bottom atmosphere is partially reflected at the base of the cloud (backscattering effects). The same is true for NERs between the upper atmosphere and the top of the dense cloud region, as well as for NERs between all the atmosphere above the dense cloud region and space. Altogether, the effect of scattering on the total radiative budget reaches 8% at the bottom and 7% at the top of the dense cloud region (Figure 9).

3. Parameterization

[34] We derive a simple parameterization of the NER matrix usable in a general circulation model. As a first step, we assume that the vertical distributions of infrared absorbers and scatterers will be kept constant with latitude and time in the first phase of Venus general circulation modeling. We therefore concentrate on the ability of the parameterization to accurately represent the effects associated with temperature changes at constant composition. Corresponding computation requirements and extension to variable compositions is then briefly discussed.

3.1. GCM Parameterization Simulations With Constant Atmospheric Composition

[35] For each NER $\Psi_{nb}(i, j)$ between elements i and j in narrow band index nb an exchange factor $\overline{\xi}_{nb}(i, j)$ is defined, following *Dufresne et al.* [2005], as

$$\overline{\xi}_{nb}(i,j) = \frac{\Psi_{nb}(i,j)}{B_{nb}(j) - B_{nb}(i)} \tag{5}$$

where $B_{nb}(i)$ and $B_{nb}(j)$ are the values of the Planck function at the mass weighted average temperatures $\overline{T}_i$ and $\overline{T}_j$ of atmospheric layers i and j respectively. The parameterization objective is then to find efficient ways of evaluating $\overline{\xi}_{nb}(i, j)$. In the case of a constant atmospheric composition, $\Psi_{nb}(i, j)$, and therefore $\overline{\xi}_{nb}(i, j)$, evolve as function of the atmospheric temperature profile only. If we further assume that temperature variations around the T^{VIRA} profile do not affect absorption and scattering cross sections, then temperature changes modify only the values of the Planck function and the sensitivity of $\overline{\xi}_{nb}(i, j)$ to temperature is strictly related to the vertical temperature profiles within atmospheric layers i and j. In such conditions, as developed in the work of *Dufresne et al.* [2005], we can argue that a high level of accuracy is met by simply assuming that $\overline{\xi}_{nb}(i, j)$ takes a constant value $\overline{\xi}^{ref}_{nb}(i, j)$. NERs are evaluated as:

$$\Psi_{nb}(i,j) \approx \overline{\xi}^{ref}_{nb}(i,j)[B_{nb}(j) - B_{nb}(i)] \tag{6}$$

which only requires two computations of the Planck function at the average temperatures. The matrix of all $\overline{\xi}^{ref}_{nb}(i, j)$ is computed once for all using the Monte Carlo code detailed in the previous section.

[36] There are three limit cases for which this approximation of a constant $\overline{\xi}_{nb}(i, j)$ may be demonstrated. The discussion assumes that i and j are atmospheric layers, but extension to cases where i or j is ground or space is straightforward:

[37] 1. when the absolute difference $|\overline{T}_i - \overline{T}_j|$ is large compared with the temperature variations within atmospheric layers i and j (which corresponds essentially to the NERs between distant layers);

[38] 2. when atmospheric layers i and j are optically thin;

[39] 3. when atmospheric layers i and j are adjacent layers and the temperature profile is linear with pressure (or quadratic for adjacent layers of identical mass).

[40] The reciprocity principle tells us that the space $\Gamma(i, j)$ of the optical paths γ from any point in atmospheric layer i to any point in atmospheric layer j is formally identical to the space $\Gamma(j, i)$ of the optical paths from any point in atmospheric layer j to any point in atmospheric layer i. This simply means that $E(i \rightarrow j)$ and $E(j \rightarrow i)$ (see equation (1)) have the same integral structure [*De Lataillade et al.*, 2002; *Eymet et al.*, 2005; *Dufresne et al.*, 1998]:

$$E(j \rightarrow i) = \int_{IR} d\nu \int_{\Gamma_{i,j}} d\gamma \xi_\nu(\gamma) B_\nu(\gamma, j) \tag{7}$$

$$E(i \rightarrow j) = \int_{IR} d\nu \int_{\Gamma_{i,j}} d\gamma \xi_\nu(\gamma) B_\nu(\gamma, i) \tag{8}$$

leading to

$$\Psi(i,j) = \int_{IR} d\nu \int_{\Gamma_{i,j}} d\gamma \xi_\nu(\gamma) [B_\nu(\gamma,j) - B_\nu(\gamma, i)] \tag{9}$$

where ν is the frequency integrated over the infrared, γ is the optical path integrated over the space $\Gamma(i, j)$, $\xi_\nu(\gamma)$ is an opticogeometric factor including absorption, scattering and surface reflection, and $B_\nu(\gamma, i)$ and $B_\nu(\gamma, j)$ are the blackbody intensities at the temperatures of the beginning and end of the optical path γ. With such a formulation the first limit case is trivial. Temperature variations within each layer can be neglected and the blackbody intensity difference $B_\nu(\gamma, j) - B_\nu(\gamma, i)$ in equation (9) can be approximated as $B_{nb}(j) - B_{nb}(i)$ (note that according to the narrow band assumption the Planck function is independent of frequency within each band):

$$\Psi_{nb}(i,j) = \int_{\Delta\nu_{nb}} d\nu \int_{\Gamma_{ij}} d\gamma \xi_\nu(\gamma) [B_\nu(\gamma,j) - B_\nu(\gamma, i)] \tag{10}$$

$$\approx \left[\int_{\Delta\nu_{nb}} d\nu \int_{\Gamma_{ij}} d\gamma \xi_\nu(\gamma) \right] [B_{nb}(j) - B_{nb}(i)] \tag{11}$$

This means that

$$\overline{\xi}_{nb}(i,j) \approx \int_{\Delta\nu_{nb}} d\nu \int_{\Gamma_{ij}} d\gamma \xi_\nu(\gamma) \tag{12}$$

which depends on optical properties only and has therefore no direct temperature dependence.

[41] For the second limit case, the reason why $\overline{\xi}_{nb}(i, j)$ may be kept constant is that radiation emitted at each location within a layer exits the layer without significant extinction. This means that the total power emitted by a layer is the same as if the layer was isothermal at a temperature corresponding to the average blackbody intensity. If the temperature heterogeneity within each layer is small, the Planck function can be linearized and the average blackbody intensity corresponds approximately to the Planck function at the average temperature.

[42] The third limit case is quite different, as no analogy can be made with the isothermal layer case. The full demonstration can be found in the work of *Dufresne et al.* [2005] and we only concentrate here on the physical pictures corresponding to the particular case of optically thick adjacent layers. As discussed in section 2.3, radiative exchanges between adjacent layers are indeed particularly important because they occur at frequencies where opacities are high. At such frequencies the NER is dominated by optical paths corresponding to radiation emitted and absorbed in the immediate vicinity of the interface between the two layers. For such optical paths γ between layer i and layer $i + 1$, let us note $P_{\gamma,i}$ and $P_{\gamma,i+1}$ the pressure at the extremities of the path located in layer i and layer $i + 1$ respectively. If $P_{\gamma,i}$ and $P_{\gamma,i+1}$ are close to the interface I the Planck function can be linearized as a function of pressure:

$$B_\nu(\gamma, i) - B_\nu(\gamma, i+1) \approx \left(\frac{\partial B_{nb}}{\partial P} \right)_I \left(P_{\gamma,i} = -P_{\gamma,i+1} \right) \tag{13}$$

and the NER becomes

$$\Psi_{nb}(i, i+1) \approx \left[\int_{\Delta\nu_{nb}} d\nu \int_{\Gamma_{i,i+1}} d\gamma \xi_\nu(\gamma) \left(P_{\gamma,i} - P_{\gamma,i+1} \right) \right] \left(\frac{\partial B_{nb}}{\partial P} \right)_I$$

Provided that $\left(\frac{\partial B_{nb}}{\partial P}\right)_I$ can be replaced by the ratio $\frac{B_{nb}(i) - B_{nb}(i+1)}{P_{c,i} - P_{c,i+1}}$, we get

$$\overline{\xi}_{nb}(i, i+1) \approx \left[\int_{\Delta\nu_{nb}} d\nu \int_{\Gamma_{i,i+1}} d\gamma \xi_\nu(\gamma) \left(P_{\gamma,i} - P_{\gamma,i+1} \right) \right] \cdot \frac{1}{P_{c,i} - P_{c,i+1}}$$

where $P_{c,i}$ and $P_{c,i+1}$ are the pressure coordinates at the center of mass of layer i and layer $i + 1$. As in the two first limit cases, $\overline{\xi}_{nb}(i, i + 1)$ appears therefore as a purely opticogeometric quantity: it is independent of temperature despite of the fact that the sublayer temperature profiles play an essential part in such exchanges. Replacing the Planck function gradient at the interface $\left(\frac{\partial B_{nb}}{\partial P}\right)_I$ by $\frac{B_{nb}(i) - B_{nb}(i+1)}{P_{c,i} - P_{c,i+1}}$ is exact if the Planck function can be linearized as function of temperature and if the temperature profile is either a linear function of P throughout the two adjacent layers (whatever layers thicknesses), or a quadratic function of pressure in the particular case where the two layers are of equal mass [*Dufresne et al.*, 2005].

[43] These three limit cases are very much meaningful for the NERs that were shown to be dominant in section 2.3: NERs between adjacent layers on the one hand, and NERs with surface, space, cloud bottom and cloud top, on the other hand, that correspond to long distance exchanges for which the first and second limit cases apply. In order to test more generally the validity of the constant $\overline{\xi}_{nb}(i, j)$ assumption for Venus applications, we computed $\overline{\xi}_b^{ref}(i, j)$ for the

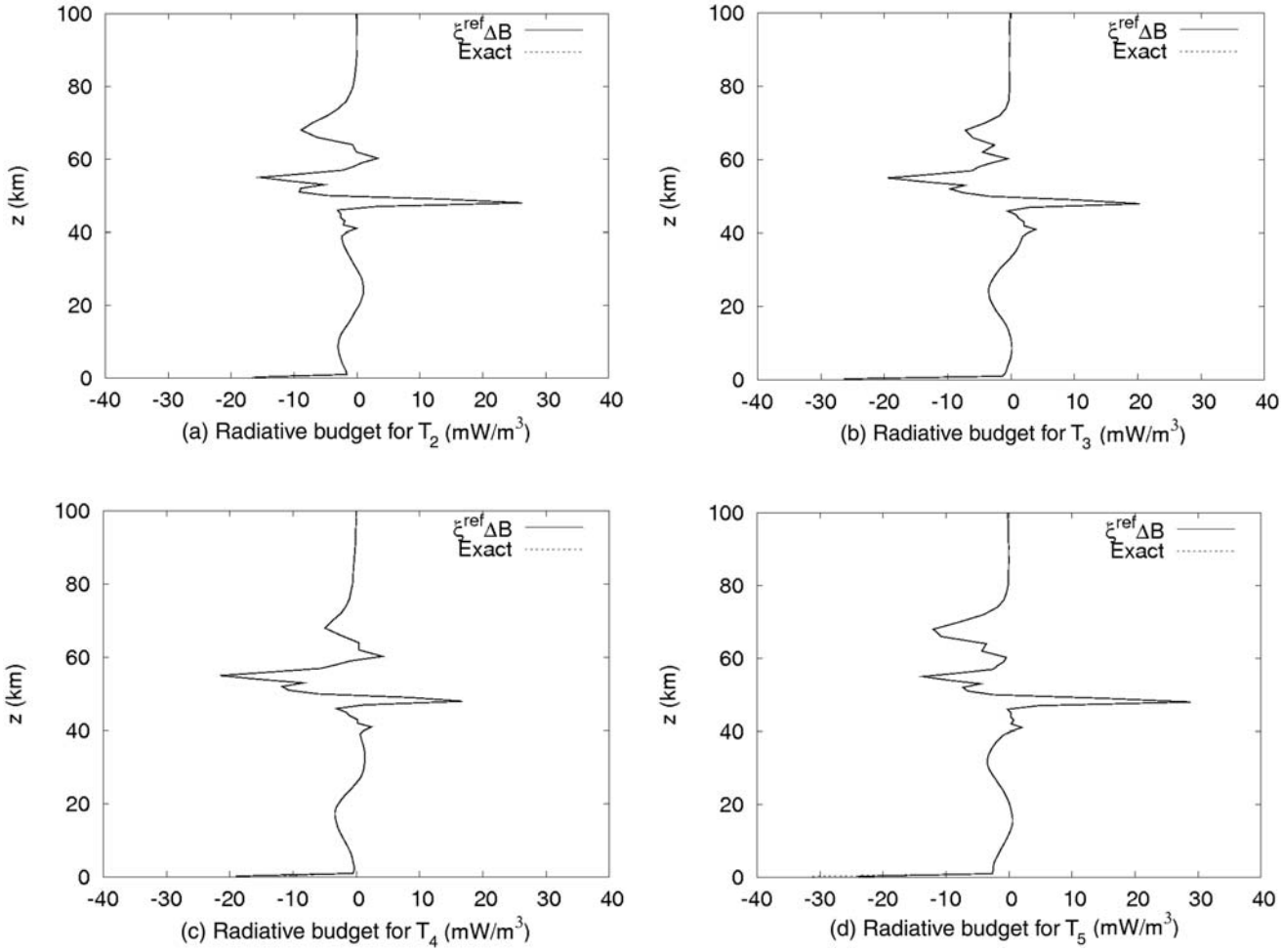

Figure 11. Radiative budget (mW/m^3) as function of altitude, ($\zeta_{nb}(i)/\Delta z_i$, where Δz_i is the thickness of layer i) for the four test temperature profiles T_2 to T_5, fixing the absorption properties to those of the reference temperature profile $T_1 = T^{\mathrm{VIRA}}$. The results labeled $\xi^{ref}\Delta B$ correspond to those of the proposed parameterization with a constant ξ^{ref} computed for $T_1 = T^{\mathrm{VIRA}}$.

VIRA profile and then computed the approximate solution (equation (6)) and the exact solution for four perturbed temperature profiles. To obtain these profiles, we added sinusoidal temperature perturbations to the smoothed VIRA profile. The amplitude of the perturbation is 10 K and the wavelength is 33 km. Four different phases are used in order to check the effects of changes in temperature and temperature gradients at all altitudes in the range of the maximum fluctuations expected in Venus GCMs: these four temperature profiles ($T_2 - T_5$) are: $T_2(z) = T^{\mathrm{VIRA}}(z) + 10 \sin\left(\frac{2\pi z}{33}\right)$, $T_3(z) = T^{\mathrm{VIRA}}(z) - 10 \sin\left(\frac{2\pi z}{33}\right)$, $T_4(z) = T^{\mathrm{VIRA}}(z) + 10 \sin\left(\frac{2\pi z}{33} - \frac{\pi}{2}\right)$, $T_5(z) = T^{\mathrm{VIRA}}(z) - 10 \sin\left(\frac{2\pi z}{33} - \frac{\pi}{2}\right)$. Figure 11 displays such comparisons, indicating that the adequation is quasi perfect at all altitudes.

[44] This parameterization is presently used in a first series of three-dimension Venus GCM simulations [*Eymet et al.*, 2006; *Crespin et al.*, 2006] based on the terrestrial LMDZ model [*Hourdin et al.*, 2006]. Such simulations include the surface pressure variations associated with orography, which means that the $\overline{\xi}^{ref}_{nb}(i, j)$ matrix is different at each latitude-longitude location. In order to avoid the computation and storage of a large number of such matrices, $\overline{\xi}^{ref}_{nb}(i, j)$ is interpolated on the basis of 96 simulations corresponding to a regular discretization of surface pressures in the 40–115 bar range (using a 5 bars step) and a discretization of the altitude at the top of the clouds in the 58–70 km range (using a 4 km step). This is widely sufficient to meet the present requirements and no further efforts were made toward storage reduction, in particular as far as the number of narrow bands is concerned.

[45] Note that in the tests performed above (Figure 11) we used infrared opacities corresponding to the reference T^{VIRA} profile. The variations of infrared opacities with temperature were therefore neglected. The effect of this approximation on cooling rates can be evaluated, in order to check whether a parameterization refinement is required, using the k distribution data built for temperature profiles shifted of +10 K and −10 K away from T^{VIRA} (see section 2.1). A reference solution is built, in which k distribution data are linearly interpolated between $T^{\mathrm{VIRA}} - 10$ K, T^{VIRA} and $T^{\mathrm{VIRA}} + 10$ K and the results are compared to the previous parameterization results. It appears that, in terms of cooling rates, opacity variations with temperature have only significant influences (≈10%) in the high atmosphere above the

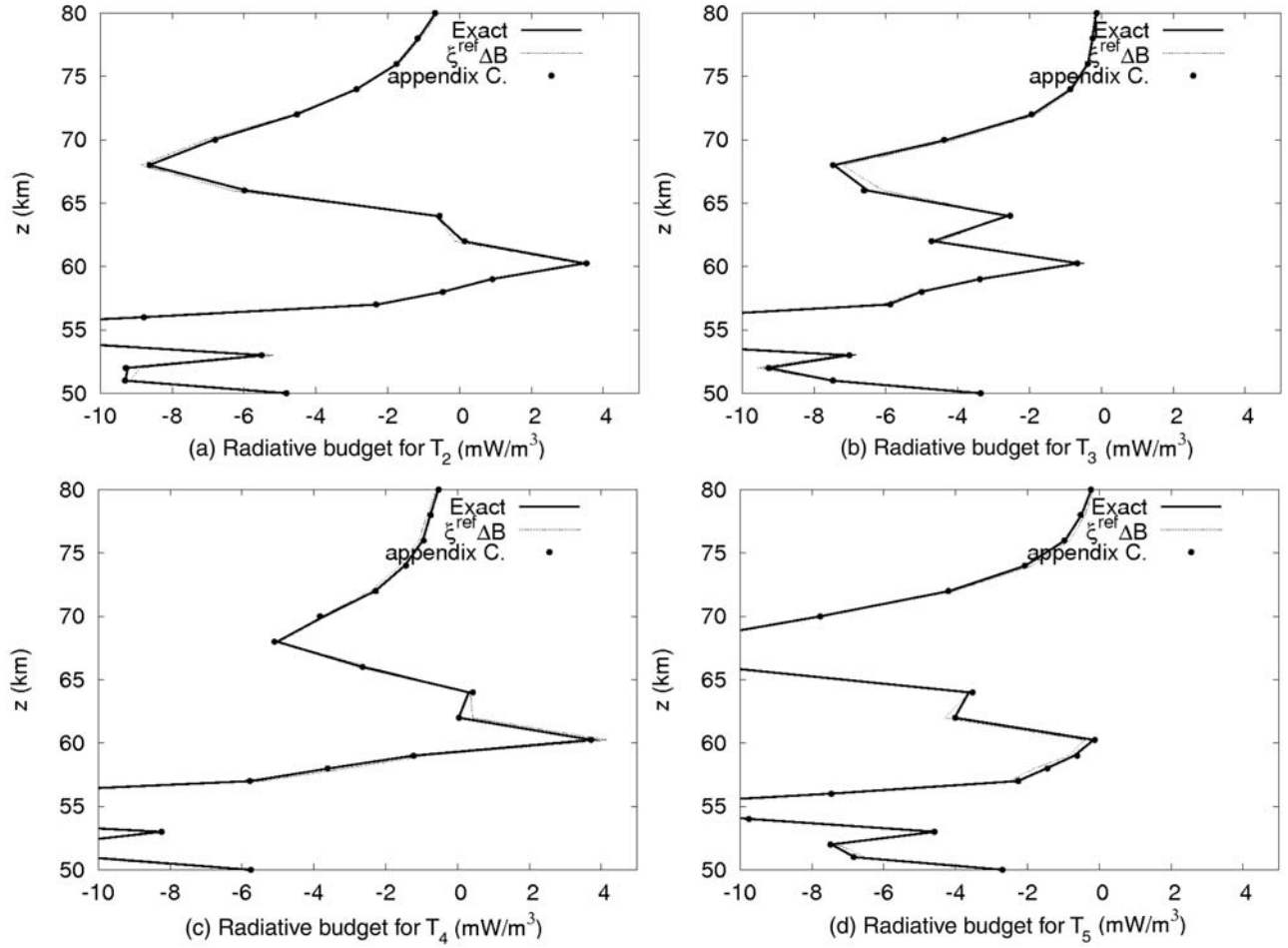

Figure 12. Same as Figure 11 above 50 km, with absorption properties function of temperature (for the exact solution, the *k* distribution data have been interpolated using the $T^{\mathrm{VIRA}} - 10$ K, T^{VIRA}, and $T^{\mathrm{VIRA}} + 10$ K). Also displayed, the results of the upgraded parameterization described in Appendix C.

clouds. A simple practical solution is detailed in Appendix C that allows the parameterization to be upgraded in order to correct this discrepancy (see Figure 12).

3.2. Computational Requirements and Extension Toward Variable Cloud Structures

[46] In the current configuration, with 68 narrow bands and 50 vertical levels, the use of this parameterization in the Venus version of LMDZ GCM, with one single NER matrix, increases the size of the model executable from roughly 360 Mo to 425 Mo. To include the surface pressure dependency, the use of 16 different matrices increases this size by roughly 23 Mo. This increase is linear with respect to the number of matrices used, which means that using N matrices would increase the size by roughly $1.5 \times N$ (in Mo). N could therefore be significantly increased above 16 without any difficulty, which will first be used to test the effect of the variations with latitude of cloud altitudes and structures.

[47] Increasing the number of NER matrices can therefore be easily used to account for spatial variations of the atmospheric composition, but a strong limitation of the present proposition is the fact that composition is assumed constant in time. In a near future, if the amounts of absorbers and scatterers (gaseous absorbers and cloud droplets) are allowed to vary along a GCM simulation, then a physical model will be required for the variation of $\overline{\xi}^{ref}_{nb}(i, j)$ with atmospheric composition. For large variations, the corresponding computational requirements will probably be very significant and the first steps will therefore be to find systematic ways of reducing the number of NERs by neglecting parts of the matrix for a given accuracy level, optimize the number of narrow bands, and linearize the blackbody intensities with temperature (which allows a summation over the narrow bands as illustrated in Appendix C) without violating the reciprocity principle. All such developments will be held successively, following the needs of the Venus GCM community, and will probably concentrate on the cloud region and the upper atmosphere.

[48] However, for small variations, simple solutions can be rapidly implemented. Each $\overline{\xi}^{ref}_{nb}(i, j)$ can indeed be linearized as function of n main parameters of the vertical distributions of absorbers and scatterers. Such an approach only requires that sensitivity matrices are computed once and stored for use in a Taylor like first order expansion. The feasibility is therefore directly related to

[49] 1. The computation time required to produce the sensitivity matrices with sufficient accuracy level,

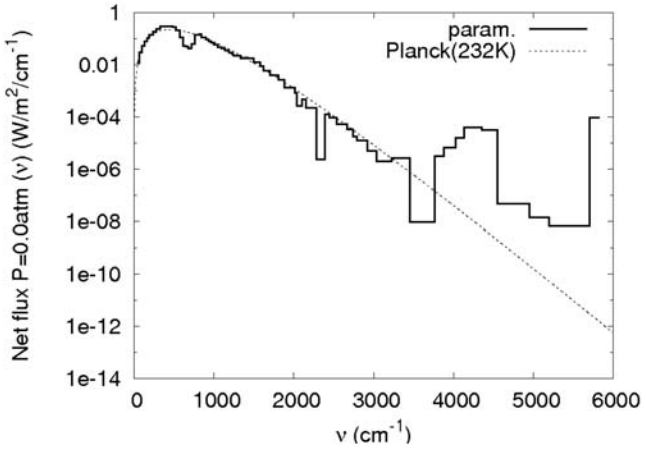

Figure 13. Net flux signal in $W/m^2/cm^{-1}$ at the top of atmosphere (P = 0.0 atm) in the [0–6000] cm^{-1} spectral range. Net flux at the top of atmosphere is compared to the Planck intensity at 232 K using a logscale.

[50] 2. The additional memory size corresponding the $n \times N$ sensitivity matrices (where, as defined above, N is the number of reference NER matrices),

[51] 3. And the computation time associated to the linear computation of each $\overline{\xi}_{nb}(i, j)$ from $\overline{\xi}^{ref}_{nb}(i, j)$ and its sensitivities to the n retained parameters.

[52] The computation of sensitivity matrices may look very demanding. It will indeed not be possible to make use of analytical formulations of the NER sensitivities, because scattering is essential in the vicinity and within the cloud, where composition variations will first be analyzed (see Figure 9 and section 2.3). Accurately computing sensitivities of infrared radiative transfer quantities with numerical tools is a well identified difficulty and very few practical solutions are available [*Weise and Zhang*, 1997]. However, it was recently shown that such sensitivities could be computed with the Monte Carlo method, in parallel to the main computation algorithm, with very little additional computation costs [*Roger et al.*, 2005]. Upgrading KARINE to compute the sensitivities of $\overline{\xi}^{ref}_{nb}(i, j)$ to the vertical composition parameters is therefore only a question of practical implementation (most of the corresponding feasibility tests have already been performed by *Roger* [2006]). Computing $n \times N$ with n and N of the order of several tens should therefore introduce no specific technical difficulty. The above reported tests indicate that the memory size increase should be of the order of $1.5 \times n \times N$ (in Mo). For the computers used in this study, a memory size of up to 2 Go would be acceptable, which allows to reach $n \times N$ values of the order of 1000. If we think of a maximum of N = 30 for variations with grid points of orography and cloud structure, this leaves us with n = 30 parameters for the vertical composition at each grid point, which should be widely sufficient for first analysis of the coupling of atmospheric dynamics with chemistry (if radiation is indeed shown to play a significant role in this coupling). In terms of computing time, the present configuration of the parameterization (with 2000 radiative iterations per Venus day) induces an increase of approximately 10% of the total computing time of the GCM. Including the sensitivities to n parameters with n of the order of several tens may increase this proportion, though this needs to be assessed.

4. Comparison With Observations and Sensitivity to the Main Free Parameters

[53] The new parameterization accuracy has been checked so far against Monte Carlo simulation results assuming that all optical data are exact and we can confidently extrapolate that the parameterization methodology will remain accurate if enhanced optical data are used in the future. The purpose of the present section is to establish the uncertainty level associated to our present data in order to allow their use in today's first series of GCM simulations.

[54] The easiest quantitative control consists in the computation of the emitted thermal radiation at the top of the atmosphere and its comparison with the incident solar flux time the integral Bond albedo. It is commonly admitted that the expected average emitted flux should be 157 ± 6 W m^{-2} [*Titov et al.*, 2007]. Using the optical data and the cloud structure described in section 2, together with the VIRA temperature profile, we obtain an emitted flux value of 156.0 W m^{-2} which is within the expected range. To further analyze this emitted thermal radiation, its spectrum is first compared in Figure 13 with the spectrum of blackbody emission at 232 K as suggested in *Bullock and Grinspoon* [2001]. In logarithmic scale, the agreement is indeed very good, except in the strong CO_2 absorption bands and at near-infrared frequencies where the H_2SO_4 clouds are translucent. The detailed spectral structure can then be compared with available observations. For the [0; 2000 cm^{-1}] wave number range, Figure 14 displays a comparison with the average spectrum corresponding to the [−10; +10] latitudes as observed during the Venera 15 mission [*Zasova et al.*, 2007]. These data are retained here because Zasova et al. used them to infer the cloud model that we retained for the present study. A high level of consistency can therefore be expected, and indeed the two spectra match quite

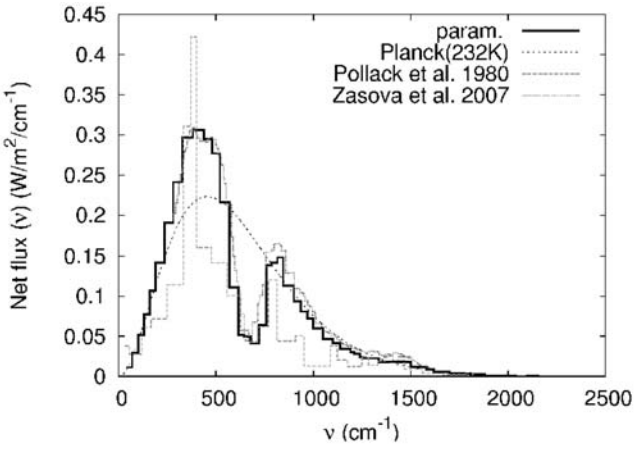

Figure 14. Net flux signal in $W/m^2/cm^{-1}$ at the top of atmosphere (P = 0.0 atm) in the [0–2500] cm^{-1} spectral range. Reference results are compared to the Planck intensity at 232 K, computational results from the work of *Pollack et al.* [1980], and observational results from the work of *Zasova et al.* [2007].

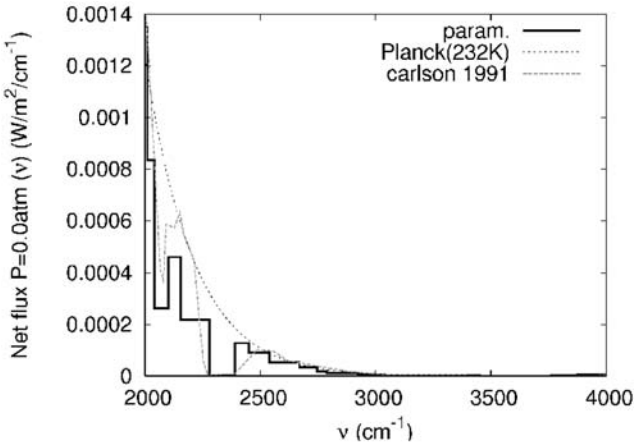

Figure 15. Net flux signal in $W/m^2/cm^{-1}$ at the top of atmosphere ($P = 0.0$ atm) in the [2000–4000] cm^{-1} spectral range. Net flux at the top of atmosphere is compared to the Planck intensity at 232 K and observational results from the work of *Carlson et al.* [1991].

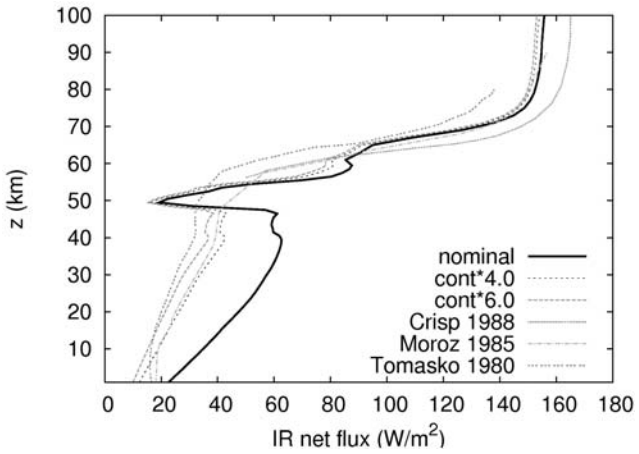

Figure 17. Net flux in W/m^2 as function of altitude for our nominal model and for continuum optical depth increased by factors 4 and 6. Solar net flux profiles from the works of *Crisp* [1986], *Moroz et al.* [1985], and *Tomasko et al.* [1980] are also displayed.

accurately. This spectral signature is also very close to that of the emitted fluxes simulated by *Crisp and Titov* [1997] and *Titov et al.* [2007] at a much higher spectral resolution. This result is not reproduced in Figure 14, but the agreement level is very much similar to that of comparisons with *Zasova et al.* [2007] results. Comparison with the simulation results of *Pollack et al.* [1980] is less satisfactory but the essential features can still be considered quite similar, keeping in mind the limits of the gaseous spectral data and the cloud models available in the early 1980s. For the [2000; 4000 cm^{-1}] wave number range, Figure 15 displays a comparison with observations performed by the NIMS instrument during the 1990 Galileo flyby of the dark side of Venus [*Carlson et al.*, 1991; *Taylor et al.*, 1997]. The agreement is not as good as in Figure 14 but is still very much satisfactory considering our poor spectral resolution in this less energetic part of the spectrum.

[55] Similar spectral comparisons could not be performed for altitude levels within the atmosphere because all available observed spectra correspond to outgoing radiation at the top of the atmosphere. We could only compare our spectra with those simulated by *Pollack et al.* [1980], as reported in Figure 16: at the level corresponding to a pressure of 0.79 atm the agreement is as partial as for the top of atmosphere flux, but again, absorption data and cloud models are quite different. Further analysis of net fluxes within the atmosphere can only be performed on a spectrally integrated basis. Figure 17 displays the integrated net flux as a function of altitude for our nominal model using VIRA temperature profile. For comparison, Figure 18 reproduces the net thermal flux derived from the SNFR and LIR measurements on Pioneer Venus descent probes, as summarized in the work of *Revercomb et al.* [1985]. The uncertainty and apparent dependence on location are such that these observations are very difficult to use for the present validation exercise. However, we can keep in mind that the order of magnitude of 100 W m^{-2} at 60 km seems to be a point of agreement, but none of the observed net flux profiles shows such a strong variation at the bottom of the cloud as what we simulate with our optical data (from 20 W m^{-2} to 60 W m^{-2} in a few kilometers when descending through the bottom of the cloud). An other discrepancy is the net flux value in the very low atmosphere: in the bottom twenty kilometers, we find net fluxes between 20 W m^{-2} and 50 W m^{-2}, whereas measurements are more in the [0; 20 W m^{-2}] range.

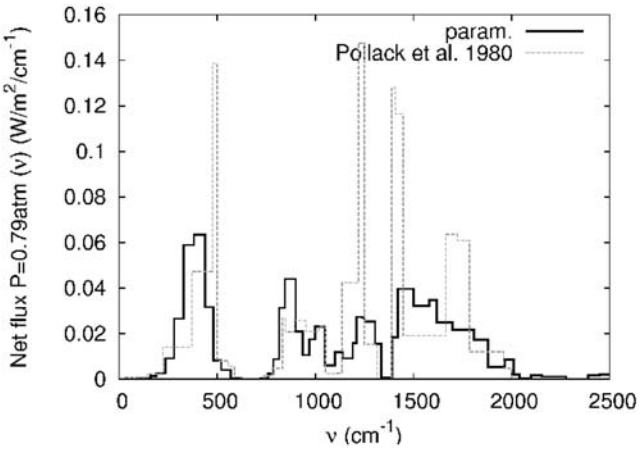

Figure 16. Net flux signal in $W/m^2/cm^{-1}$ at a pressure of 0.79 atm (around 53 km altitude) in the [0–2500] cm^{-1} spectral range. Simulation results are compared to the computational result of the work of *Pollack et al.* [1980].

[56] This raises the question of continuum adjustment. The CO_2 continuum model that we are using is very much uncertain. Some constraints are available in the near-infrared windows, but at all other frequencies, specifications of the continuum can only be addressed through modeling attempts, without any experimental control. Collision induced continuums are much better understood for Earth-like conditions, but the pressure levels (92 bars) and the typical exchange distances (1 km) encountered in the deep Venus atmosphere are so high that no laboratory experiment is able to reproduce comparable conditions. The collision induced continuum is therefore essentially unknown in the energeti-

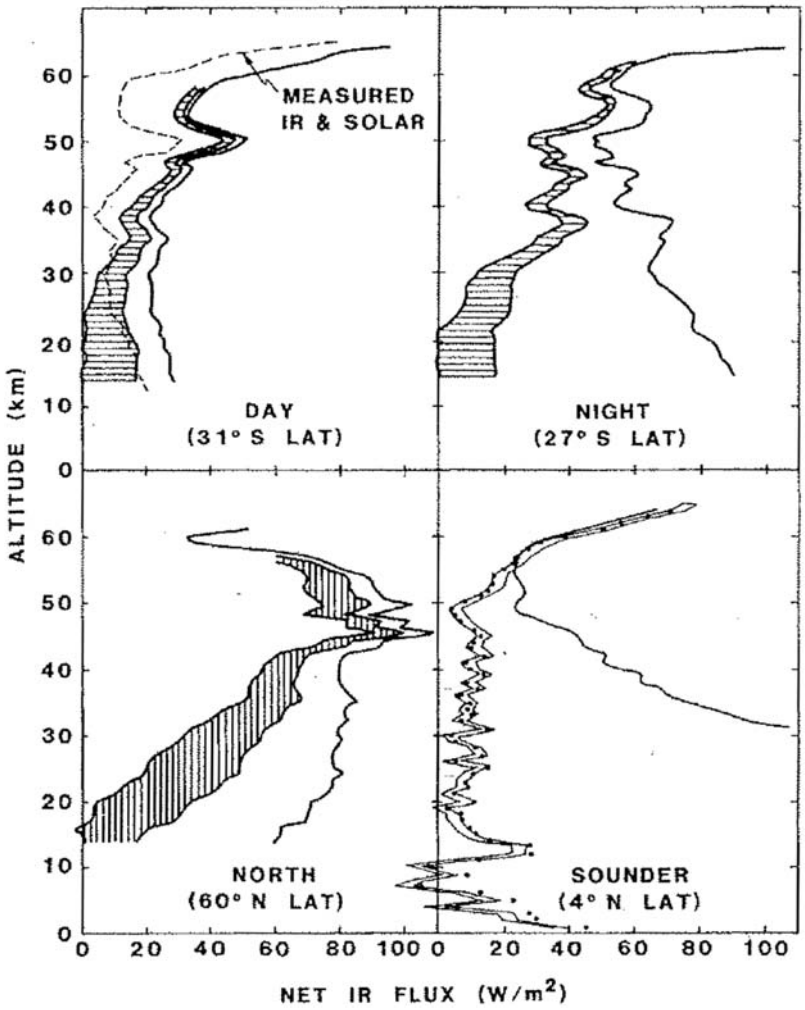

Figure 18. Thermal net flux profiles (W/m^2) from the work of *Revercomb et al.* [1985].

cally dominant part of the spectrum. Furthermore, the far wing sub-Lorentzian shapes of absorption lines at such pressures is also very much unknown and this induces a continuum-like uncertainty that cannot be distinguished from the collision induced continuum. Some kind of continuum adjustment is therefore required in any radiative simulation. Despite of the measurement uncertainties, the above described comparison of simulated and observed net flux vertical profiles can help us in this adjustment exercise. In Figure 17, simulated net flux profiles are reported that correspond to various scaling factors applied to our continuum model at all frequencies below 4030 cm^{-1}. The continuum is kept unchanged at near infrared frequencies because this is the only frequency range for which the continuum can be constrained on the basis of observed emitted spectra at the top of the atmosphere (and we indeed checked that our continuum values were consistent with the values used by *Bézard et al.* [1990] in the 1.73 and 2.30 μm spectral windows). The conclusions of this sensitivity test to the continuum model is that we need to increase continuum absorption by a factor as high as 6 if we want that the integrated net flux be lower than 20 W m^{-2} at 20 km. Doing so, the net flux profile is only weakly modified within and above the cloud, but the strong net flux variation at the bottom of the cloud is considerably reduced, which leads to a better agreement with descent probes observations.

[57] The other available data within the atmosphere are the observed and simulated solar net fluxes. In first approximation, these can be related to the thermal net fluxes provided that convection processes and atmospheric transport are negligible. Convection processes are assumed to play a role within the cloud and at some locations in the deep atmosphere and atmospheric transport is systematically mentioned when attempting to analyze the observed latitudinal temperature contrasts. However, at most latitudes/altitudes, except within the cloud, it remains very much meaningful to think of Venus atmosphere as in a state of radiative equilibrium, or quite close to radiative equilibrium. The detailed analysis of such processes is one of the objectives of GCM simulations, but we still briefly compare here, in Figure 17 the thermal net flux profiles corresponding to our nominal model (with the original continuum and the continuum increased by a factor 4 and then 6) with three global mean net solar fluxes from the literature [*Tomasko et al.*, 1980; *Moroz et al.*, 1985; *Crisp*, 1986]. All three thermal net flux profiles are compatible with 157 ± 6 W m^{-2} at the top of the atmosphere. A convection zone is clearly visible between 48 and 55 km, since the thermal net flux is lower

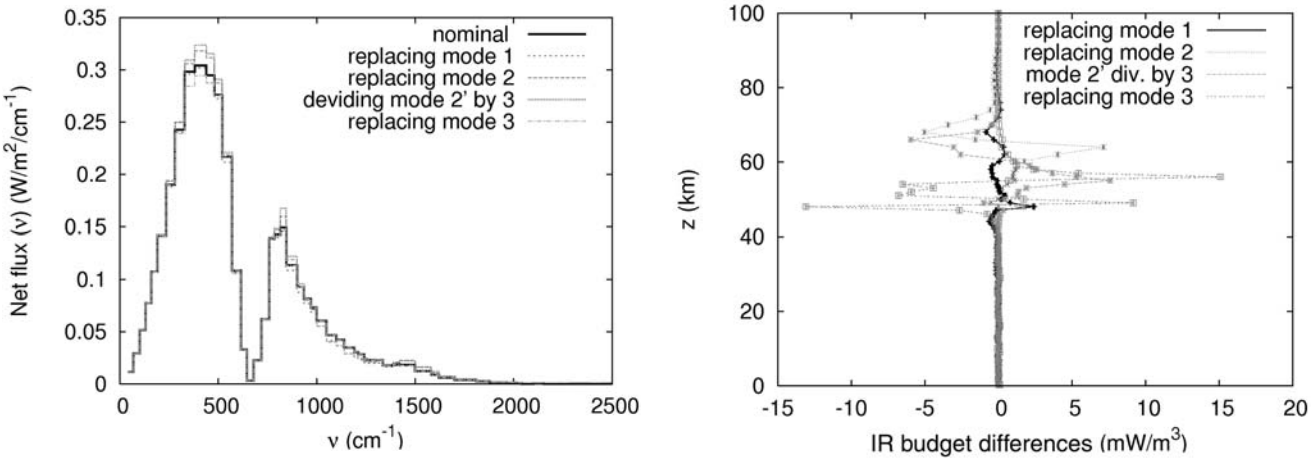

Figure 19. Sensitivites of (a) top of atmosphere flux signal and (b) radiative budget to cloud model. Nominal modal radiuses and standard deviations, as well as particle concentration, from the work of *Zasova et al.* [2007] for modes 1, 2, and 3 have been replaced by data from the work of *Knollenberg and Hunten* [1980]. Nominal particle concentration for mode 2′ have been divided by a factor 3.

than the expected solar net flux. Orders of magnitude between solar and thermal net fluxes are comparable in the lower atmosphere (below 48 km) when continuum absorption optical depths are adequately adjusted. Note that, should the continuum optical depth be multiplied by a factor 4 or 6, a convection zone would appear in the ten first kilometers. Finally, differences between thermal and solar net fluxes are clearly visible in the 55–65 km zone, which may be due to the fact that different cloud models were used for solar fluxes computations, or to three-dimensional circulation effects, which would imply that reasoning on the basis of a latitudinally averaged solar net flux profile is meaningless.

[58] Apart from collision-induced absorption, the most significant free parameters are the parameters of the cloud model. These parameters are constrained by top of atmosphere fluxes as well as in situ observations of particle sizes and shapes along descent probes trajectories. However, these constraints leave strong uncertainties concerning particle size distributions and vertical density profiles, particularly at high latitudes where the cloud structure can be considered as virtually unknown. A systematic sensitivity analysis cannot be among the objectives of the present paper and we therefore only discuss four sensitivity tests: successively, each particle mode of our nominal cloud model (that of *Zasova et al.* [2007]) is replaced by that of *Knollenberg and Hunten* [1980]. Mode 2 particles exist only in the high cloud in the work of *Zasova et al.* [2007], whereas they are present throughout the whole cloud in the work of *Knollenberg and Hunten* [1980]. Therefore the curve labeled "replacing mode 2" was obtained with a cloud model where mode 2 particles have been taken from the work of *Knollenberg and Hunten* [1980] for altitudes higher than 65 km only. Since there is no mode 2′ particles in the work of *Knollenberg and Hunten* [1980], the curve labeled "mode 2′ divided by 3" has been obtained with a cloud model where nominal mode 2′ cumulated optical depths at 0.63 μm, at 48 km ($\tau_{0.63\mu m}$ = 14.26) have been scaled to match the data presented in the work of *Tomasko et al.* [1985] ($\tau_{0.63\mu m}$ = 4.66 at 48 km), which required that mode 2′ particle densities were divided by a factor three. The result of these tests, displayed in Figure 19, indicate that sensitivites of the thermal net flux at the top of the atmosphere are quite small. The largest differences (less than 10%) are obtained when modifying mode 2 and 2′ properties. Figure 19b displays the differences between the radiative budget corresponding to the modified clouds on the one hand and the nominal radiative budgets of Figure 9a on the other hand. Sensitivities to the cloud model are much larger in terms of radiative budgets than in terms of top of the atmosphere fluxes: differences are approximately 20% for modes 1, 2 and 2′, and reach 50% for mode 3. These impacts are concentrated in the cloud region and may significantly modify the convective structure, and the details of the general circulation in the 40–70 km altitude range. It is therefore important to consider introducing the dependency of the NER coefficients to cloud parameters, together with the coupling of a microphysical model describing the cloud structure within the GCM.

5. Conclusion and Perspectives

[59] Major progress in our understanding of planetary atmospheric systems require that ground based or spatial observations are accompanied by the development of comprehensive models, which because of the complexity and non linearity of the atmospheric dynamics and physics, can generally be achieved only through the development of physically based numerical tools such as the so-called General Circulation Models. One major step in the development of such models is the derivation of "radiative transfer parameterizations," i.e., highly simplified but accurate enough versions of the full radiative transfer calculation. This major step in general, becomes a real challenge in the extreme venusian case, with in particular its deep CO_2 atmosphere and highly scattering clouds.

[60] We have presented in the present paper the process of the development of the radiative transfer code which is presently operational in the LMD venusian GCM. Several results have been achieved during this long process:

[61] 1. It was first practically demonstrated that most recent Monte Carlo algorithms were able to accurately simulate infrared radiative transfer in such an optically thick system as Venus atmosphere (in terms of both absorption and scattering). Because of their integral nature, the NERs considered in the present work could only be evaluated with integral radiative transfer solvers, and among them only the Monte Carlo algorithms can deal with low Knudsen multiple scattering. This step was therefore essential.

[62] 2. The Venus NER matrices were carefully analyzed prior to any parameterization attempt. We believe that the corresponding physical pictures may provide useful insights to Venus radiative transfer, particularly when attempting to analyze the coupling of radiation with atmospheric dynamics.

[63] 3. An essential point was the quantification of the impact of the main remaining uncertainty sources. We concentrated on collision induced continuum and cloud particle vertical distributions, for which we show that significant changes in optical properties may have little impacts on the well constrained top of atmosphere fluxes, but strong impacts on very much unknown radiative energy exchanges as well as radiation-convection vertical coupling. The fact that few direct observations are available concerning continuum absorption and detailed cloud structures leaves strong degrees of freedom that must be translated into adjustable parameters when trying to reproduce Venus vertical thermal structure and atmospheric dynamics with a general circulation model.

[64] 4. When exploring optical data available in the literature, we observed that it was very difficult to distinguish between differences that are worth a detailed physical interpretation attempt, and differences that are only the consequences of inversion procedure uncertainties. This can be easily explained by the strong difficulties associated to the understanding of such a complex physical system as Venus atmosphere. Obviously the state of the art is undeniably more advanced and clearer as far as near-infrared windows are concerned, but we can state that detailed general circulation analysis will require that strong further efforts be made toward the representation of optical properties throughout the whole infrared at all altitudes.

[65] 5. Finally, at our given stage of knowledge, we have shown that it was possible to derive, thanks to the NER approach, and despite the extreme conditions encountered in the venusian atmosphere, a fast and accurate parameterization usable in a GCM. Of course, the methodology can be used to update the radiative code, as soon as new information becomes available on the venusian atmospheric composition, microphysical cloud properties and optical properties.

[66] Until now, the code was only derived for a fixed atmospheric composition and for thermal radiation only. Accounting to first order to the space time variations of clouds or composition is not a major issue, and should be considered in the future, when the question will arise from the climate studies. We are currently working on the derivation of a code for the shortwave radiation.

Appendix A: Spectral Mesh

[67] Table A1.

Table A1. Spectral Limits of the 68 Narrow Bands

Band Index	Lower λ (μm)	Upper λ (μm)	Lower ν (cm^{-1})	Upper ν (cm^{-1})
1	1.717	1.755	5699.62	5825.00
2	1.755	1.923	5200.12	5699.62
3	1.923	2.020	4950.37	5200.12
4	2.020	2.198	4549.75	4950.37
5	2.198	2.299	4349.95	4549.75
6	2.299	2.418	4134.86	4349.95
7	2.418	2.481	4029.87	4134.86
8	2.481	2.581	3874.92	4029.87
9	2.581	2.660	3759.73	3874.92
10	2.660	2.899	3449.84	3759.73
11	2.899	3.101	3224.55	3449.84
12	3.101	3.289	3040.04	3224.55
13	3.289	3.419	2924.85	3040.04
14	3.419	3.584	2790.30	2924.85
15	3.584	3.642	2745.44	2790.30
16	3.642	3.745	2670.01	2745.44
17	3.745	3.938	2539.53	2670.01
18	3.938	4.082	2449.82	2539.53
19	4.082	4.185	2389.68	2449.82
20	4.185	4.387	2279.58	2389.68
21	4.387	4.640	2155.22	2279.58
22	4.640	4.762	2100.17	2155.22
23	4.762	4.902	2040.03	2100.17
24	4.902	4.974	2010.47	2040.03
25	4.974	5.090	1964.60	2010.47
26	5.090	5.319	1879.99	1964.60
27	5.319	5.526	1809.65	1879.99
28	5.526	5.884	1699.56	1809.65
29	5.884	6.173	1620.04	1699.56
30	6.173	6.328	1580.29	1620.04
31	6.328	6.668	1499.76	1580.29
32	6.668	7.041	1420.24	1499.76
33	7.041	7.196	1389.66	1420.24
34	7.196	7.493	1334.62	1389.66
35	7.493	7.663	1305.05	1334.62
36	7.663	8.000	1250.01	1305.05
37	8.000	8.066	1239.81	1250.01
38	8.066	8.263	1210.25	1239.81
39	8.263	8.404	1189.86	1210.25
40	8.404	8.773	1139.91	1189.86
41	8.773	9.090	1100.16	1139.91
42	9.090	9.522	1050.21	1100.16
43	9.522	9.997	1000.26	1050.21
44	9.997	10.31	969.677	1000.26
45	10.31	10.69	935.018	969.677
46	10.69	11.11	900.359	935.018
47	11.11	11.83	845.313	900.359
48	11.83	12.27	814.731	845.313
49	12.27	12.74	785.169	814.731
50	12.74	13.16	759.685	785.169
51	13.16	13.89	719.929	759.685
52	13.89	14.70	680.173	719.929
53	14.70	15.52	644.494	680.173
54	15.52	16.26	614.932	644.494
55	16.26	17.54	570.079	614.932
56	17.54	19.23	520.130	570.079
57	19.23	20.82	480.374	520.130
58	20.82	22.75	439.598	480.374
59	22.75	26.28	380.474	439.598
60	26.28	30.35	329.505	380.474
61	30.35	35.77	279.555	329.505
62	35.77	42.61	234.702	279.555
63	42.61	52.67	189.849	234.702
64	52.67	62.39	160.287	189.849
65	62.39	77.10	129.706	160.287
66	77.10	99.86	100.144	129.706
67	99.86	143.8	69.5621	100.144
68	143.8	250.0	40.0000	69.5621

Appendix B: Clouds Optical Properties

[68] The lognormal distribution used for describing cloud droplets size distributions in this article is $n(r) = N_0 p(r)$, where N_0 is the nominal particle density and the probability density function p is defined as

$$p(r) = \frac{1}{\sqrt{2\pi}.r.\sigma_{\log}} \exp\left[-\frac{1}{2}\left(\frac{\ln\left(\frac{r}{\bar{r}}\right)}{\sigma_{\log}}\right)^2\right] \tag{B1}$$

where $\bar{r}$ is the modal radius and $\sigma_{\log}$ is the logarithmic width. The effective radius r_e is defined as: $r_e = \frac{\langle r^3 \rangle}{\langle r^2 \rangle}$, with:

$$\langle r^2 \rangle = \int_0^{+\infty} p(r) r^2 dr = \bar{r}^2 \exp\left(2\ln(\sigma)^2\right) \tag{B2}$$

$$\langle r^3 \rangle = \int_0^{+\infty} p(r) r^3 dr = \bar{r}^3 \exp\left(\frac{9}{2}\ln(\sigma)^2\right) \tag{B3}$$

leading to:

$$r_e = \bar{r}.\exp\left(\frac{5}{2}\ln(\sigma)^2\right) \tag{B4}$$

[69] A program based on the Mie scattering theory is used in order to compute extinction efficiency factors q_{ext}, single-scattering albedos ω and asymmetry parameters g as functions of wave number, for each particle mode. The microphysical parameters are:

[70] 1. The lognormal distribution parameters for each particle mode, from the works of *Knollenberg and Hunten* [1980] and *Grinspoon et al.* [1993] (see Tables 1 and 2).

[71] 2. The mass percentage of H_2SO_4 for each particle mode [*Knollenberg and Hunten*, 1980] (see Table 1).

[72] 3. The complex refractive index of H_2SO_4 solutions, as function of wave number, from the work of *Palmer and Williams* [1975].

[73] The extinction optical depth τ_{ext} of a given atmospheric layer, for a given particle mode, is:

$$\tau_{ext} = \frac{3}{4}\frac{q_{ext}.M}{\rho.r_e} \tag{B5}$$

where ρ is the particle volumic mass and M is the surfacic mass corresponding to the particles in the considered layer (that extends from z_1 to z_2), that can be computed as $M(z_1, z_2) = \rho\frac{4}{3}\pi < r^3 > \int_{z_1}^{z_2} N_0(z)dz$, which leads to $\tau_{ext} = \pi q_{ext}\bar{r}^2\exp(2\ln^2(\sigma)) \int_{z_1}^{z_2} N_0(z)dz$.

[74] The absorption τ_a and scattering τ_s optical depths for the considered particle mode are $\tau_s = \tau_{ext}\omega$ and $\tau_a = (1-\omega)\tau_{ext}$. Total optical depths for each layer are the sum of the contributions of all particle modes.

Appendix C: Simple Upgrades for the Upper Atmosphere

[75] Upgrading the parameterization in order to include opacity variations with temperature is widely simplified by the fact that scattering has only a little influence on infrared radiative transfers above the clouds (Figures 9 and 10). All NERs involving atmospheric layers above the clouds can be accurately modeled under the absorption approximation. This means that the analytical form of each $\overline{\xi}_{nb}(i,j)$ can be partially derived as function of each temperature $\bar{T}_p$ to produce analytical expressions of the sensitivities $\frac{\partial\overline{\xi}^{ref}_{nb}(i,j)}{\partial\bar{T}_p}$ around T^{VIRA} for each layer index p between i and j. A linear expansion of $\overline{\xi}_{nb}(i,j)$ can then be used to derive the following upgraded version of the parameterization:

$$\Psi_{nb}(i,j) \approx \left[\overline{\xi}^{ref}_b(i,j) + \sum_{p=\min(i,j)}^{\max(i,j)} \frac{\partial\overline{\xi}^{ref}_{nb}(i,j)}{\partial\bar{T}_p}\left(\bar{T}_p - \bar{T}^{ref}_p\right)\right] \cdot (B_{nb}(j) - B_{nb}(i)) \tag{C1}$$

[76] Before any accuracy test, we first checked that the linear expansion induces no violation of the reciprocity principle, meaning that whatever the nonlinearities of $\overline{\xi}_{nb}(i,j)$ with temperature (opacities are linearly interpolated but extinctions are exponential) $\overline{\xi}^{ref}_{nb}(i,j) + \sum_p \frac{\partial\overline{\xi}^{ref}_{nb}(i,j)}{\partial\bar{T}_p}\left(\bar{T}_p - \bar{T}^{ref}_p\right)$ remains positive for all i, j and nb in the considered perturbation range. For the four sinusoidal perturbations described above, no such difficulty was encountered. Results in terms of cooling rates indicate that the opacity variations are well reproduced with such a parameterization (not shown).

[77] However, the partial derivatives $\frac{\partial\overline{\xi}^{ref}_{nb}(i,j)}{\partial\bar{T}_p}$ require a much larger storage than $\overline{\xi}^{ref}_{nb}(i,j)$ which is a severe handicap. A first practical solution is to make use of equation (C1) only for the dominant NERs (NERs with space, with the two adjacent layers, and with one or two layers at the top of the cloud) and to keep the standard parameterization for the remaining NERs. However, this still leads to a factor 4 or a factor 5 increase of the storage requirement. This can be reduced by linearizing the Planck function for the correction term:

$$\begin{aligned}\Psi_{nb}(i,j) \approx{}& \overline{\xi}^{ref}_{nb}(i,j)(B_{nb}(j) - B_{nb}(i)) \\ &+ \left[\sum_{p=0}^{m+1} \frac{\partial\overline{\xi}^{ref}_{nb}(i,j)}{\partial\bar{T}_p}\left(\bar{T}_p - \bar{T}^{ref}_p\right)\right] \\ &* \left[B^{ref}_{nb}(j) + \frac{\partial B^{ref}_{nb}(j)}{\partial\bar{T}_j}\left(\bar{T}_j - \bar{T}^{ref}_j\right)\right. \\ &\left. - B^{ref}_{nb}(i) - \frac{\partial B^{ref}_{nb}(i)}{\partial\bar{T}_i}\left(\bar{T}_i - \bar{T}^{ref}_i\right)\right]\end{aligned}$$

This allows to sum once over the narrow bands before applying the perturbation:

$$\begin{aligned}\Psi(i,j) ={}& \sum_{nb=1}^{N_b} \Psi_{nb}(i,j) \\ \approx{}& \sum_{nb=1}^{N_b} \overline{\xi}^{ref}_{nb}(i,j)(B_{nb}(j) - B_{nb}(i)) \\ &+ \sum_{p=0}^{m+1}\left(\bar{T}_p - \bar{T}^{ref}_p\right)\left[A^{ref}_{i,j,p} + C^{ref}_{i,j,p}\left(\bar{T}_j - \bar{T}^{ref}_j\right)\right. \\ &\left. - D^{ref}_{i,j,p} - E^{ref}_{i,j,p}\left(\bar{T}_i - \bar{T}^{ref}_i\right)\right]\end{aligned}$$

with

$$A^{ref}_{i,j,p} = \sum_{nb=1}^{N_b} \frac{\partial \overline{\xi}^{ref}_{nb}(i,j)}{\partial \bar{T}_p} B^{ref}_{nb}(j) \quad \text{(C2)}$$

$$C^{ref}_{i,j,p} = \sum_{nb=1}^{N_b} \frac{\partial \overline{\xi}^{ref}_{nb}(i,j)}{\partial \bar{T}_p} \frac{\partial B^{ref}_{nb}(j)}{\partial \bar{T}_j} \quad \text{(C3)}$$

$$D^{ref}_{i,j,p} = \sum_{nb=1}^{N_b} \frac{\partial \overline{\xi}^{ref}_{nb}(i,j)}{\partial \bar{T}_p} B^{ref}_{nb}(i) \quad \text{(C4)}$$

$$E^{ref}_{i,j,p} = \sum_{nb=1}^{N_b} \frac{\partial \overline{\xi}^{ref}_{nb}(i,j)}{\partial \bar{T}_p} \frac{\partial B^{ref}_{nb}(i)}{\partial \bar{T}_i} \quad \text{(C5)}$$

As these last four coefficients do not depend on the narrow band index, if only the dominant NERs are considered, then the storage requirement is very small compared to that of $\overline{\xi}^{ref}_{nb}(i,j)$. Such a parameterization upgrade is therefore easy to implement.

[78] However, as soon as the temperature perturbations are of the same order as the difference $|\bar{T}_j - \bar{T}_i|$ (which can commonly occur for layers close the one to the other), this approximation can easily lead to a violation of the reciprocity principle. Nothing ensures indeed that the difference $B^{ref}_{nb}(j) + \frac{\partial B^{ref}_{nb}(j)}{\partial \bar{T}_j}(\bar{T}_j - \bar{T}^{ref}_j) - B^{ref}_{nb}(i) - \frac{\partial B^{ref}_{nb}(i)}{\partial \bar{T}_i}(\bar{T}_i - \bar{T}^{ref}_i)$ is positive when $\bar{T}_j$ is greater than $\bar{T}_i$. This solution can therefore only be applied to long distance net exchanges. In practice, we only used it for net exchanges with space. It could certainly be used for net exchanges with the top of the clouds, for layers far enough from the cloud, but we could not yet think of a systematic enough procedure.

[79] For adjacent layers, a simpler procedure can be implemented. The temperature difference between adjacent layers can indeed be assumed to be small enough so that the Planck function can be linearized around the same temperature for the two layers. This leads to

$$\begin{aligned}\Psi(i,i+1) &= \sum_{nb=1}^{N_b} \Psi_{nb}(i,i+1) \\ &\approx \sum_{nb=1}^{N_b} \overline{\xi}^{ref}_{nb}(i,i+1)(B_{nb}(i+1) - B_{nb}(i)) \\ &\quad + \sum_{p=i}^{i+1} F^{ref}_{i,i+1,p}\left(\bar{T}_p - \bar{T}^{ref}_p\right)(\bar{T}_{i+1} - \bar{T}_i)\end{aligned} \quad \text{(C6)}$$

with

$$F^{ref}_{i,i+1,p} = \sum_{nb=1}^{N_b} \frac{\partial \overline{\xi}^{ref}_{nb}(i,i+1)}{\partial \bar{T}_p} \frac{1}{2}\left(\frac{\partial B^{ref}_{nb}(i)}{\partial \bar{T}_i} + \frac{\partial B^{ref}_{nb}(i+1)}{\partial \bar{T}_{i+1}}\right) \quad \text{(C7)}$$

The fact that the difference $(\bar{T}_{i+1} - \bar{T}_i)$ appears directly in the expression of the correction terms insures that the reciprocity principle is satisfied whatever the temperature perturbation profile.

[80] **Acknowledgments.** This work has been supported by the Centre National d'Etudes Spatiales (CNES). V.E. acknowledges support from ESA 18134/04/NL/LVH/GM and from the postdoctoral fellowship program of CNES. M.B. acknowledges support from NASA Planetary Atmospheres grant NNG06GD61G.

References

Allen, D., and J. Crawford (1984), Cloud structure on the dark side of Venus, *Nature*, *307*, 222–224.

Belyaev, D., O. Korablev, A. Fedorova, J.-L. Bertaux, A.-C. Vandaele, F. Montmessin, A. Mahieux, V. Wilquet, and R. Drummond (2008), First observations of SO_2 above Venus' clouds by means of solar occultation in the infrared, *J. Geophys. Res.*, *113*, E00B25, doi:10.1029/2008JE003143.

Bézard, B., and C. de Bergh (2007), Composition of the atmosphere of Venus below the clouds, *J. Geophys. Res.*, *112*, E04S07, doi:10.1029/2006JE002794.

Bézard, B., C. de Bergh, D. Crisp, and J. Maillard (1990), The deep atmosphere of Venus revealed by high-resolution nightside spectra, *Nature*, *345*, 508–511.

Blanco, S., and R. Fournier (2003), An invariance property of diffusive random walks, *Europhys. Lett.*, *61*(2), 168–173.

Bullock, M. (1997), The stability of climate on Venus, Ph.D. thesis, Univ. of Colorado, Boulder, Colo.

Bullock, M., and D. Grinspoon (2001), The recent evolution of climate on Venus, *Icarus*, *150*, 19–37.

Burch, D., D. Gryvnak, R. Patty, and C. Bartky (1969), Absorption of infrared radiant energy by CO_2 and H_2O: IV. Shapes of collision-broadened CO_2 lines, *J. Opt. Soc. Am.*, *59*, 267–280.

Carlson, R., et al. (1991), Galileo infrared imaging spectroscopy measurements at Venus, *Science*, *253*, 1541–1548.

Cherkaoui, M., J.-L. Dufresne, R. Fournier, J. Y. Grandpeix, and A. Lahellec (1996), Monte-Carlo simulation of radiation in gases with a narrow-band model and a net-exchange formulation, *ASME J. Heat Trans.*, *118*, 401–407.

Crespin, A., S. Lebonnois, F. Hourdin, V. Eymet, R. Fournier, and F. Forget (2006), An infrared radiative transfer parameterization for a Venus General Circulation Model, in *DPS Meeting 2006*, *Bull. Am. Astron. Soc.*, *38*(3), 515.

Crisp, D. (1986), Radiative forcing of the Venus mesosphere, *Icarus*, *67*, 484–514.

Crisp, D., and D. Titov (1997), The thermal balance of the Venus atmosphere, in *Venus II*, edited by S. W. Bougher, D. M. Hunten, and R. J. Phillips, pp. 353–384, Univ. of Arizona Press, Tucson, Ariz.

de Bergh, C., V. I. Moroz, F. W. Taylor, D. Crisp, B. Bézard, and L. V. Zasova (2006), The composition of the atmosphere of Venus below 100 km altitude: An overview, *Planet. Space Sci.*, *54*, 1389–1397.

De Lataillade, A., J.-L. Dufresne, M. El Hafi, V. Eymet, and R. Fournier (2002), A net exchange Monte-Carlo approach to radiation in optically thick systems, *J. Quant. Spectrosc. Radiat. Trans.*, *74*, 563–584.

Dufresne, J.-L., R. Fournier, and J. Y. Grandpeix (1998), Méthode de Monte-Carlo par échanges pour le calcul des bilans radiatifs au sein d'une cavité 2D remplie de gaz, *C. R. Acad. Sci., Paris, Ser. IIb*, *326*, 33–38.

Dufresne, J., C. Hourdin, R. Fournier, and F. Hourdin (2005), Net exchange reformulation of radiative transfer in the CO_2 15 μm band on Mars, *J. Atmos. Sci.*, *62*, 3303–3319.

Esposito, L., R. Knollenberg, M. Marov, O. Toon, and R. Turco (1983), The clouds and hazes of Venus, in *Venus*, edited by D. M. Hunten et al., pp. 484–564, Univ. of Arizona Press, Tucson, Ariz.

Eymet, V., J. Dufresne, P. Ricchiazzi, R. Fournier, and S. Blanco (2004), Longwave radiative analysis of cloudy scattering atmospheres using a net exchange formulation, *Atmos. Res.*, *72*, 238–261.

Eymet, V., J. Dufresne, R. Fournier, and S. Blanco (2005), A boundary-based net exchange Monte-Carlo Method for absorbing and scattering thick medium, *J. Quant. Spectrosc. Radiat. Trans.*, *95*, 27–46.

Eymet, V., R. Fournier, S. Lebonnois, M. Bullock, J.-L. Dufresne, and F. Hourdin (2006), An infrared radiative transfer parameterization for a Venus General Circulation Model, in *DPS Meeting 2006*, *Bull. Am. Astron. Soc.*, *38*(3), 527.

Fedorova, A., et al. (2008), HDO and H_2O vertical distributions and isotopic ratio in the Venus mesosphere by solar occultation at infrared spectrometer on board Venus Express, *J. Geophys. Res.*, *113*, E00B22, doi:10.1029/2008JE003146.

Forget, F., F. Hourdin, R. Fournier, C. Hourdin, O. Talagrand, M. Collins, S. Lewis, P. Read, and J. Huot (1999), Improved general circulation models of the Martian atmosphere from the surface to above 80 km, *J. Geophys. Res.*, *104*(E10), 24,155–24,175.

Goody, R., and Y. Yung (1995), *Atmospheric Radiation: Theoretical Basis*, Oxford Univ. Press, New York.

Goody, R., R. West, L. Chen, and D. Crisp (1989), The correlated-k method for radiation calculations in nonhomogeneous atmospheres, *J. Quant. Spectrosc. Radiat. Trans.*, *42*(6), 539–550.

Green, J. S. A. (1967), Division of radiative streams into internal transfer and cooling to space, *Q. J. R. Meteorol. Soc.*, *93*, 371–372.

Grinspoon, D., J. Pollack, B. Sitton, R. Carlson, L. Kamp, K. Baines, T. Encrenaz, and F. Taylor (1993), Probing Venus' cloud structure with Galileo NIMS, *Planet. Space Sci.*, *41*, 515–542.

Gruszka, M., and A. Borysow (1997), Roto-translational collision-induced absorption of CO_2 for the atmosphere of Venus at frequencies from 0 to 250 cm^{-1} and at temperature from 200 K to 800 K, *Icarus*, *129*, 172–177.

Hourdin, F., O. Talagrand, R. Sadourny, R. Courtin, D. Gautier, and C. McKay (1995), General circulation of the atmosphere of Titan, *Icarus*, *117*, 358–374.

Hourdin, F., et al. (2006), The LMDZ4 General Circulation Model: Climate performance and sensitivity to parametrized physics with emphasis on tropical convection, *Clim. Dyn.*, *19*, 3445–3482.

Joseph, J., and R. Bursztyn (1976), A radiative cooling model in the thermal infrared for application to models of the general circulation, *J. Appl. Meteorol.*, *15*, 319–325.

Knollenberg, R., and D. Hunten (1980), The microphysics of the clouds of Venus: Results of the Pioneer Venus particle size spectrometer experiment, *J. Geophys. Res.*, *85*(A13), 8039–8058.

Lacis, A. A., and V. Oinas (1991), Description of the correlated-*k* distribution method for modeling nongray gaseous absorption, thermal emission, and multiple scattering in vertically inhomogeneous atmospheres, *J. Geophys. Res.*, *96*(D5), 9027–9063.

Lebonnois, S., F. Hourdin, V. Eymet, R. Fournier, and J.-L. Dufresne (2005), A new Venus General Circulation Model in the context of the Venus-Express mission, in *DPS Meeting 2005*, *Bull. Am. Astron. Soc.*, *37*(3), 742.

Lebonnois, S., A. Crespin, F. Hourdin, V. Eymet, R. Fournier, and J.-L. Dufresne (2006), Super-rotation simulated with the new LMD Venus General Circulation Model, in *EGU General Assembly 2006*, *Geophys. Res. Abstracts*, vol. 8, p. 06006, Vienna, Austria.

Marcq, E., B. Bézard, P. Drossart, G. Piccioni, J. M. Reess, and F. Henry (2008), A latitudinal survey of CO, OCS, H_2O, and SO_2 in the lower atmosphere of Venus: Spectroscopic studies using VIRTIS-H, *J. Geophys. Res.*, *113*, E00B07, doi:10.1029/2008JE003074.

Moroz, V., A. Ekonomov, B. Moshkin, H. Revercomb, L. Sromovsky, J. Schofield, D. Spnkuch, M. Taylor, and F. W. Tomasko (1985), Solar and thermal radiation in the Venus atmosphere, *Adv. Space Res.*, *5*(11), 197–232.

Moskalenko, N., Y. Il'in, S. Parzhin, and L. Rodionov (1979), Pressure-induced IR radiation absorption in atmospheres, *Izvestiya, Atmos. Oceanic Phys.*, *15*, 632–637.

Palmer, K., and D. Williams (1975), Optical constants of sulfuric acid: Application to the clouds of Venus?, *Appl. Opt.*, *14*, 208–219.

Perrin, M., and J. Hartmann (1989), Temperature-dependant measurements and modeling of absorption by CO_2-N_2 mixtures in the far line-wings of the 4.3 μm CO_2 band, *J. Quant. Spectrosc. Radiat. Trans.*, *42*, 311–317.

Pollack, J., D. Strecker, F. Witteborn, E. Erickson, and B. Baldwin (1978), Properties of the clouds of Venus, as inferred from airborne observations of its near infrared reflectivity spectrum, *Icarus*, *34*, 28–45.

Pollack, J., O. Toon, and R. Boese (1980), Greenhouse models of Venus' high surface temperature, as constrained by Pioneer Venus measurements, *J. Geophys. Res.*, *85*(A13), 8223–8231.

Revercomb, H., L. Sromovsky, V. Suomi, and R. Boese (1985), Net thermal radiation in the atmosphere of Venus, *Icarus*, *61*, 521–538.

Richardson, M. I., A. D. Toigo, and C. E. Newman (2007), PlanetWRF: A general purpose, local to global numerical model for planetary atmospheric and climate dynamics, *J. Geophys. Res.*, *112*, E09001, doi:10.1029/2006JE002825.

Roberts, E., J. Selby, and L. Biberman (1976), Infrared continuum absorption by atmospheric water vapor in the 8–12 μm window, *Appl. Opt.*, *15*, 2085–2090.

Roger, M. (2006), Modèles de sensibilité dans le cadre de la mèthode de Monte-Carlo: Illustrations en transfert radiatif, Ph.D. thesis, Thèse de doctorat, Insitut National Polytechnique de Toulouse, Toulouse, France.

Roger, M., S. Blanco, M. El Hafi, and R. Fournier (2005), Monte Carlo estimates of domain-deformation sensitivities, *Phys. Rev. Lett.*, *95*(18), 180601, doi:10.1103/Phys.RevLett.95.180601.

Rothman, L., et al. (2000), HITEMP, the high-temperature molecular spectroscopic database. (Available at http://www.hitran.com)

Rothman, L., et al. (2003), The HITRAN molecular spectroscopic database: Edition of 2000 including updates of 2001, *J. Quant. Spectrosc. Radiat. Trans.*, *82*, 1–4.

Schubert, G. (1983), General circulation and the dynamical state of the Venus atmosphere, in *Venus*, edited by D. M. Hunten et al., pp. 681–765, Univ. of Arizona Press, Tucson, Ariz.

Taylor, F., D. Crisp, and B. Bézard (1997), Near-infrared sounding of the lower atmosphere of Venus, in *Venus II*, edited by S. W. Bougher, D. M. Hunten, and R. J. Phillips, pp. 325–351, Univ. of Arizona Press, Tucson, Ariz.

Titov, D. V., M. A. Bullock, D. Crisp, N. O. Renno, F. W. Taylor, and L. V. Zasova (2007), Radiation in the atmosphere of Venus, in *Exploring Venus as a Terrestrial Planet*, *Geophys. Monogr. Ser.*, vol. 176, edited by L. W. Esposito, E. R. Stofan, and T. E. Cravens, pp. 121–138, AGU, Washington, D. C.

Tomasko, M., L. Doose, P. Smith, and A. Odell (1980), Measurements of the flux of sunlight in the atmosphere of Venus, *J. Geophys. Res.*, *85*(A13), 8167–8186.

Tomasko, M., L. Doose, and P. Smith (1985), The absorption of solar energy and the heating rate in the atmosphere of Venus, *Adv. Space Res.*, *5*(9), 71–79.

von Zahn, U., and V. Moroz (1985), Composition of the Venus atmosphere below 100 km altitude, *Adv. Sp. Res.*, *5*, 173–195.

Washburn, E., C. West, and N. Dorsey (1930), *International Critical Tables of Numerical Data, Chemistry and Technology*, Mc Graw Hill, National Research Council, New York.

Weise, K., and H. Zhang (1997), Uncertainty treatment in Monte-Carlo simulation, *J. Phys. A*, *30*, 5971–5980.

Zasova, L., N. Ignatiev, I. Khatuntsev, and V. Linkin (2007), Structure of the Venus atmosphere, *Planet. Space Sci.*, *55*, 1712–1728.

M. A. Bullock, Department of Space Studies, Southwest Research Institute, 1050 Walnut Street, Suite 300, Boulder, CO 80302, USA.

J.-L. Dufresne, F. Hourdin, and S. Lebonnois, Laboratoire de Météorologie Dynamique (LMD/IPSL), Tour 45-55, 3eme, Jussieu, CNRS/UPMC - Boite 99, F-75252 Paris cedex 05, France.

V. Eymet and R. Fournier, Laboratoire Plasma et Conversion de l'Energie (LAPLACE), UMR 5213, CNRS-UPS, Batiment 3R1, Université Paul Sabatier, 118 Route de Narbonne, 31062 Toulouse cedex 09, France. (v.eymet@gmail.com)